

Accurate estimation of functional brain connectivity via Bayesian ICA with population-derived priors

Amanda Mejia^{1,*}, David Bolin², Daniel A. Spencer¹, and Ani Eloyan³

¹Department of Statistics, Indiana University, Bloomington, IN, USA

²Statistics Program, Computer, Electrical and Mathematical Sciences and Engineering Division, King Abdullah University of Science and Technology, Thuwal, Saudi Arabia

³Department of Biostatistics, Brown University, Providence, RI, USA

*Corresponding Author, e-mail: afmejia@iu.edu

Abstract

Estimation of brain functional connectivity (FC) is essential for understanding the functional organization in the brain and for identifying changes occurring due to neurological disorders, development, treatment, and other phenomena. Independent component analysis (ICA) is a matrix decomposition method that has been used extensively for estimation of brain functional networks and their FC. However, estimation of FC via ICA is often sub-optimal due to the use of ad-hoc methods or need for temporal dimension reduction prior to traditional ICA methods. Bayesian ICA methods can avoid dimension reduction, produce more accurate estimates, and facilitate inference via posterior distributions on the model parameters. In this paper, we propose a novel, computationally efficient Bayesian ICA method with population-derived priors on both the temporal covariance, representing FC, and the spatial components of the model. We propose two algorithms for parameter estimation: a Bayesian Expectation-Maximization algorithm with a Gibbs sampler at the E-step, and a more computationally efficient variational Bayes algorithm. Through extensive simulation studies using realistic fMRI data generation mechanisms, we evaluate the performance of the proposed methods and compare them with existing approaches. Finally, we perform a comprehensive evaluation of the proposed methods using fMRI data from over 400 healthy adults in the Human Connectome Project. Our analyses demonstrate that the proposed Bayesian ICA methods produce highly accurate measures of functional connectivity and spatial brain features. The proposed framework is computationally efficient and applicable to single-subject analysis, making it potentially clinically viable.

Keywords: functional magnetic resonance imaging, fMRI, EM-algorithm, Variational Bayes, neuroimaging

1 Introduction

The widespread availability of functional magnetic resonance imaging (fMRI) technology for obtaining high-resolution images of brain function non-invasively has made it possible to study the function and organization of the human brain in ever increasing detail. One of the techniques that has proven most useful in this context is independent component analysis (ICA; Hyvarinen et al., 2002). First introduced for blind source separation, ICA is a matrix factorization method for estimating latent spatial signals using the blood oxygen level dependent (BOLD) signals from fMRI data (McKeown et al., 1998; Beckmann et al., 2005). The spatial independent components (ICs) are believed to represent brain “networks”, or collections of locations that tend to activate in a coordinated manner. By estimating these networks we can identify, for instance, differences in brain network localization between populations of interest.

While early ICA fMRI studies focused primarily on the spatial ICs, ICA can also be used to study brain functional connectivity (FC) or temporal synchrony. FC is based on the covariance of the “mixing matrix” containing the time courses corresponding to each independent component (van de Ven et al., 2004). In contrast to the traditional use of anatomical (e.g. Tzourio-Mazoyer et al., 2002) or functional brain atlases (e.g. Schaefer et al., 2018) in FC analyses, ICA deconstructs connectivity into between- and within-network components, providing a richer and more nuanced picture of brain organization (Joel et al., 2011). In addition, ICA has greater flexibility to capture the overlapping, continuous nature of brain functional topography, unlike deterministic atlases with hard boundaries (Bijsterbosch et al., 2019). ICA has been used in a range of scientific investigations to yield new insights into FC, advancing the study of autism spectrum disorder (Assaf et al., 2010; Nebel et al., 2014), Alzheimer’s disease (Greicius et al., 2004; Li et al., 2012), and major depression (Greicius et al., 2007), among others. While the scientific utility of ICA-based FC is clear, there is a need for more methodological research in this area, since historically ICA methods have focused on estimation of spatial ICs, with the mixing matrix being somewhat of an afterthought.

One of the historical limitations of non-parametric (e.g. Hyvarinen et al., 2002) and likelihood-based (Guo and Pagnoni, 2008; Eloyan et al., 2013; Guo and Tang, 2013; Risk et al., 2019) ICA methods is the assumption of a square and invertible mixing matrix. With few exceptions (e.g., Risk et al., 2019), there are few ICA methods where the underlying weight matrix is allowed to be non-square. As a result, most ICA methods require dimension reduction via PCA prior to model fitting. The full temporal activation profile associated with each IC is obtained by projecting back to the full temporal dimension. This may not provide optimal estimation of the time courses associated with the spatial ICs or their FC.

Bayesian ICA techniques can address this limitation by avoiding the need to invert the unmixing matrix, thereby allowing for rectangular mixing matrices and avoiding dimension reduction (Knuth, 1998; Mohammad-Djafari, 2001; Lawrence and Bishop, 2000). Bayesian approaches for ICA additionally facilitate inference on the spatial and/or temporal brain measures based on the posterior distributions of the model parameters. However, fitting hierarchical Bayesian ICA models to high-dimensional fMRI data may be computationally demanding or even impossible. Computationally efficient Bayesian ICA techniques are needed to provide more accurate FC estimation versus standard ICA methods that require a square mixing matrix, while being feasible and practical for fMRI analysis.

We previously proposed a computationally efficient Bayesian ICA approach for fMRI data using known population brain networks and subject-specific topographic deviations modeled as latent variables (Mejia et al., 2020). Here, we extend that model by incorporating multivariate priors on the temporal activity, where the prior covariance represents the FC between brain networks. We use population data to determine a semi-informative prior on the covariance to encode expected patterns of FC. This builds on our earlier work, where we used population priors to constrain the spatial configuration of brain networks. Here we use both sources of prior population information (spatial and temporal) to further guide and inform the ICA model.

A key scientific advantage of the proposed methods is the ability to estimate the unique spatial functional topography of an individual subject and the temporal patterns and connectivity associated with that topography. Recent neuroimaging studies have shown that the use of group-average atlases produces biased FC estimates, given the spatial misalignment between group-

level functional areas and those of a particular subject Bijsterbosch et al. (2018). In addition, this can compromise the validity of observed associations between FC and behavior, given that topographic differences are themselves biologically relevant (Kong et al., 2019; Bijsterbosch et al., 2018, 2019; Li et al., 2019; Farahibozorg et al., 2021; Li et al., 2022; Cui et al., 2020). Our proposed ICA techniques can effectively disentangle functional topography and FC to provide an accurate picture of functional brain organization and its relationship to disease, development, and interventions. Importantly, the proposed techniques are applicable to typical 10-15 minute fMRI experiments and do not require collecting hours of data on individuals (Laumann et al., 2015; Gordon et al., 2017; Braga and Buckner, 2017) to combat the high noise levels present in fMRI data.

The remainder of this manuscript is organized as follows. In Section 2 we present the proposed model. We derive a Gibbs-within-EM algorithm and an efficient VB algorithm for maximum-a-posteriori estimation of all unknown model parameters. In Section 3 we present extensive realistic simulation studies to evaluate the performance of the proposed methods and compare them to existing approaches. In Section 4 we apply the proposed methods to fMRI data from over 400 subjects from the Human Connectome Project (HCP, Van Essen et al., 2013) to further evaluate their performance and show their feasibility and practicality in real fMRI studies. We conclude with a discussion in Section 5.

2 Methods

In this section we introduce our proposed method, which we call “FC template ICA”. We employ the following notation for matrices, vectors and scalars: \mathbf{A} indicates a matrix, \mathbf{a} indicates a column vector, and a indicates a scalar. Depending on context, \mathbf{a}_i denotes the transposed i th row or the i th column of \mathbf{A} ; $a_{i,j}$ denotes the (i,j) th element of \mathbf{A} ; a_i denotes the i th element of \mathbf{a} .

Let \mathbf{Y} be a $T \times V$ matrix representing the observed BOLD fMRI data, where V is the number of brain locations (volumetric voxels or surface vertices), and T is the number of fMRI time points. In matrix form, the traditional probabilistic ICA model is given by $\mathbf{Y} = \mathbf{AS} + \mathbf{E}$, where

\mathbf{S} is a $Q \times V$ matrix, each row of which represents one of Q spatially independent components. \mathbf{A} is the $T \times Q$ unmixing matrix, which in this context represents the temporal activity of each IC during the fMRI session. The elements of \mathbf{E} are assumed to be independent Gaussian noise. Let \mathbf{a}_t represent the t th row of \mathbf{A} , and let \mathbf{s}_v represent the v th column of \mathbf{S} . The first level of the FC template ICA model at voxel $v = 1, \dots, V$ and time point $t = 1, \dots, T$ is

$$y_{tv} = \mathbf{a}_t^\top \mathbf{s}_v + e_{tv}, \text{ where } e_{tv} \sim N(0, \tau_v^2). \quad (1)$$

At the second level, we model the unmixing matrix \mathbf{A} and the ICs \mathbf{S} using population-derived priors. Following our earlier ‘‘template ICA’’ approach (Mejia et al., 2020), IC q at voxel v is modeled as

$$s_{qv} = s_{qv}^0 + \delta_{qv}, \text{ where } \delta_{qv} \sim N(0, \sigma_{qv}^2). \quad (2)$$

Since our goals include estimation of FC, we propose a further decomposition of the unmixing matrix. We consider each row \mathbf{a}_t a random vector of length Q . In the context of functional connectivity, we are interested in estimating the $Q \times Q$ covariance \mathbf{G} .

$$\mathbf{a}_t = \boldsymbol{\alpha} + \mathbf{b}_t, \text{ where } \mathbf{b}_t \sim MVN_Q(\mathbf{0}, \mathbf{G}) \quad (3)$$

The $\boldsymbol{\alpha} = (\alpha_1, \dots, \alpha_Q)^\top$ are the independent component-specific averages over time, while the $\mathbf{b}_t = (b_{t1}, \dots, b_{tQ})^\top$ capture the variation over time. Since functional connectivity is estimated by the covariance of unmixing vectors \mathbf{a}_t , the $Q \times Q$ matrix \mathbf{G} is the parameter of interest. We assume the functional connectivity covariance matrix follows an Inverse Wishart (IW) prior distribution.

$$\mathbf{G} \sim IW(\boldsymbol{\Psi}_0, \nu_0), \quad (4)$$

where the parameters $\boldsymbol{\Psi}_0$ and ν_0 are derived from the population, as described below. Finally, we assume uninformative inverse gamma (IG) priors on the likelihood noise variance τ_v^2 and uninformative normal priors on the mixing intercept $\boldsymbol{\alpha}$, namely

$$\tau_v^2 \sim IG(\alpha_0, \beta_0) \quad \text{and} \quad \alpha_q \sim N(0, \sigma_\alpha^2). \quad (5)$$

The full model is therefore given by

$$\begin{aligned}
y_{tv} &= \mathbf{a}_t^\top \mathbf{s}_v + \mathbb{E}_{tv}, \text{ where } \mathbb{E}_{tv} \sim N(0, \tau_v^2) \\
s_{qv} &= s_{qv}^0 + \delta_{qv}, \text{ where } \delta_{qv} \sim N(0, \sigma_{qv}^2) \\
\mathbf{a}_t &= \boldsymbol{\alpha} + \mathbf{b}_t, \text{ where } \mathbf{b}_t \sim MVN_Q(\mathbf{0}, \mathbf{G}) \\
\mathbf{G} &\sim InverseWishart(\boldsymbol{\Psi}_0, \nu_0) \\
\tau_v^2 &\sim InverseGamma(\alpha_0, \beta_0) \\
\alpha_q &\sim N(0, \sigma_\alpha^2).
\end{aligned}$$

While the proposed model is a novel approach to estimation of ICA-based FC, the framework is constructed of prior distributions commonly used for similar model components elsewhere (i.e. the IW prior is often used for precision matrices (Nydic, 2012), while the IG is a commonly used prior for variance components).

2.1 Population-Derived Priors

For the prior on the elements of \mathbf{S} , we estimate the prior parameters (the mean and variance) based on a training dataset, representing the population from which the focal subject comes. This process has been described previously in Mejia et al. (2020) and is implemented in the `templateICAR` R package available on CRAN. In short, we utilize test-retest fMRI data from a (preferably large) set of subjects or, in the absence of multiple sessions, we create pseudo-test-retest data by splitting the time series into two halves. We assume access to a set of group-average ICA maps, which can be either provided by established studies like the HCP (Van Essen et al., 2013) or estimated from the training data using standard software like MELODIC (Beckmann and Smith, 2004) or GIFT (Calhoun et al., 2001). We perform dual regression, a popular ad-hoc method, to obtain noisy estimates of the subject- and session-specific IC maps. We then perform a variance decomposition to obtain a non-negative estimate of the between-subject variance of each IC at each cortical vertex. This non-negative estimate contains a positive bias that converges to zero as the amount of fMRI data for each subject goes to infinity.

For the prior on the elements of \mathbf{A} , we require the parameters of the inverse Wishart hyperprior

on the covariance, namely $\Psi_0 \in \mathbb{R}^{Q \times Q}$ and $\nu_0 > Q + 1$. We estimate these parameters via a method of moments approach using a training set (as for the empirical prior on \mathbf{S}). The details of this procedure are described in Appendix A. We use a conservative estimate of the parameter controlling the variance to avoid an overly informative prior. Briefly, we utilize the subject-specific IC time courses produced from dual regression and compute an FC matrix using Pearson correlation for each subject. Using the empirical mean and variance of those FC matrices, we estimate ν_0 by minimizing the difference between the IW variance and the empirical variance, while not underestimating the empirical variance for any FC pair. As an ad-hoc measure to produce a less informative prior, we may scale the estimate of ν by some value $\lambda < 1$ to obtain $\hat{\nu}_0$. We then estimate Ψ_0 as $\hat{\Psi}_0 = \bar{\mathbf{X}}(\hat{\nu}_0 - Q - 1)$, where $\bar{\mathbf{X}}$ is the empirical mean of FC. Note that here we do not separate the within- and between-subject variability, because FC is known to vary within a subject across sessions. We therefore allow the prior to reflect both within-subject and between-subject variability.

Ideally, we would have access to a large training set of subjects to determine the prior parameters, possibly from a large publicly available fMRI dataset. There are many such datasets focused on different populations, including the HCP (Van Essen et al., 2013), the UK Biobank (Sudlow et al., 2015), the adolescent brain cognitive development (ABCD) study (Casey et al., 2018), the autism brain imaging data exchange (ABIDE; Di Martino et al., 2014), the Alzheimer’s Disease Neuroimaging Initiative (ADNI; Mueller et al., 2005), and others. It is important that the focal subject can be assumed to be drawn from the same population as the training subjects. If a separate training dataset is not available, a holdout portion of the focal study can also be used to obtain the prior parameters, assuming enough subjects are available to produce reasonably accurate parameter estimates. As a last resort, the same subjects can be used for parameter estimation and model estimation. This reduces to an empirical Bayesian framework, with the associated risks of over-fitting and under-estimation of posterior variances.

2.2 Model Estimation

We consider two estimation strategies to balance the statistical properties of the estimators with computational efficiency: an expectation-maximization (EM) algorithm with a Gibbs sampler

at the E-step to estimate posterior moments involving \mathbf{A} and \mathbf{S} , building on our previous work, and a variational Bayes (VB) algorithm based on assuming the joint posterior factorizes over \mathbf{S} , \mathbf{A} , \mathbf{G} , $\boldsymbol{\alpha}$, and the noise variance.

2.2.1 Gibbs-within-EM

We propose a Bayesian EM algorithm with a Gibbs sampler at the E-step. The M-step has an analytical solution, as do the conditional posteriors required for the Gibbs sampler within the E-step. Let $\Theta = \{\boldsymbol{\alpha}, \mathbf{G}, \{\tau_v^2\}_v\}$ denote the unknown model parameters, while \mathbf{A} and \mathbf{S} are the unknown latent variables. Given a set of parameter estimates $\hat{\Theta}$, in the E-step we determine the posterior distribution of \mathbf{S} conditional on \mathbf{A} , and the posterior distribution of \mathbf{A} conditional on \mathbf{S} . We iterate between updating \mathbf{A} and \mathbf{S} to draw samples from their joint posterior distribution. Based on those samples, we estimate the necessary posterior moments. In the M-step, we determine MAP estimates of all parameters in Θ by maximizing the expected posterior distribution of the parameters. This Bayesian EM is a simple extension of the traditional approach of maximizing the expected log-likelihood (Dempster et al., 1977). The M-step and E-step are performed repeatedly until convergence of the parameter estimates.

Here we summarize the derivation of the algorithm, with details given in Appendix A. The log-posterior for the parameters Θ , given the latent variables \mathbf{S} and \mathbf{A} , is

$$\begin{aligned} \log p(\Theta|\mathbf{Y}, \mathbf{S}, \mathbf{A}) &= \log p(\mathbf{Y}|\mathbf{A}, \mathbf{S}, \Theta) + \log p(\mathbf{S}) + \log p(\mathbf{A}|\Theta) + \log p(\Theta) \\ &= \sum_{v=1}^V \sum_{t=1}^T \log g(y_{tv} : \mathbf{a}_t^\top \mathbf{s}_v, \tau_v^2) + \sum_{v=1}^V \sum_{q=1}^Q \log g(s_{qv} : s_{qv}^0, \sigma_{qv}^2) + \sum_{t=1}^T \log g(\mathbf{a}_t : \boldsymbol{\alpha}, \mathbf{G}) \\ &\quad + \log f_{IW}(\mathbf{G} : \boldsymbol{\Psi}_0, \nu_0) + \sum_{q=1}^Q \log g(\boldsymbol{\alpha} : \mathbf{0}, \sigma_\alpha^2 \mathbf{I}) + \sum_{v=1}^V \log f_{IG}(\tau_v^2 : \alpha_0, \beta_0), \end{aligned}$$

where $g(\cdot : \boldsymbol{\mu}, \boldsymbol{\Sigma})$ denotes the Gaussian density, $f_{IW}(\cdot : \boldsymbol{\Psi}, \nu)$ denotes the IW density, and $f_{IG}(\cdot : \alpha, \beta)$ denotes the IG density.

E-step: The expected value of the log-posterior of the parameters given their values in the

previous iteration step is defined as follows.

$$Q(\Theta|\hat{\Theta}^{(k)}) = \mathbb{E} [p(\Theta|\mathbf{Y}, \mathbf{S}, \mathbf{A})] \propto Q_1(\Theta|\hat{\Theta}^{(k)}) + Q_2(\Theta|\hat{\Theta}^{(k)}),$$

where $Q_1(\Theta|\hat{\Theta}^{(k)})$ contains the terms involving τ_v^2 and $Q_2(\Theta|\hat{\Theta}^{(k)})$ contains the terms involving $\boldsymbol{\alpha}$ and \mathbf{G} . Each expectation below is over the conditional posterior of (\mathbf{S}, \mathbf{A}) , given the current parameter estimates $\hat{\Theta}^{(k)}$ at iteration k .

$$\begin{aligned} Q_1(\Theta|\hat{\Theta}^{(k)}) &\propto -\frac{T}{2} \sum_{v=1}^V \log(\tau_v^2) - \sum_{v=1}^V \frac{1}{2\tau_v^2} \sum_{t=1}^T \left\{ y_{tv}^2 - 2y_{tv} \mathbb{E} [\mathbf{a}_t^\top \mathbf{s}_v] + \mathbb{E} [(\mathbf{a}_t^\top \mathbf{s}_v)^2] \right\} \\ &\quad - (\alpha_0 + 1) \sum_{v=1}^V \log(\tau_v^2) - \beta_0 \sum_{v=1}^V \frac{1}{\tau_v^2} \end{aligned}$$

and

$$\begin{aligned} Q_2(\Theta|\hat{\Theta}^{(k)}) &\propto -\text{Tr} \left\{ \mathbf{G}^{-1} \sum_{t=1}^T \mathbb{E} [\mathbf{a}_t \mathbf{a}_t^\top] \right\} + 2\boldsymbol{\alpha}^\top \mathbf{G}^{-1} \sum_{t=1}^T \mathbb{E} [\mathbf{a}_t] - T\boldsymbol{\alpha}^\top \mathbf{G}^{-1} \boldsymbol{\alpha} \\ &\quad - (T + \nu_0 + Q + 1) \log |\mathbf{G}| - \text{Tr} \{ \boldsymbol{\Psi}_0 \mathbf{G}^{-1} \} - \frac{\boldsymbol{\alpha}^\top \boldsymbol{\alpha}}{\sigma_\alpha^2} \end{aligned}$$

M-step: The MAP estimates of the unknown parameters at iteration $k + 1$ are

$$\begin{aligned} \hat{\tau}_v^{2(k+1)} &= \frac{1}{T + 2(\alpha_0 + 1)} \left\{ \sum_{t=1}^T \left(y_{tv}^2 - 2y_{tv} \mathbb{E} [\mathbf{a}_t^\top \mathbf{s}_v] + \mathbb{E} [(\mathbf{a}_t^\top \mathbf{s}_v)^2] \right) + 2\beta_0 \right\} \\ \hat{\boldsymbol{\alpha}}^{(k+1)} &= \left(\frac{1}{\sigma_\alpha^2} \mathbf{I} + T\mathbf{G}^{-1} \right)^{-1} \mathbf{G}^{-1} \sum_{t=1}^T \mathbb{E} [\mathbf{a}_t] \\ \hat{\mathbf{G}}^{(k+1)} &= (T + \nu_0 + Q + 1)^{-1} \left\{ \sum_{t=1}^T \mathbb{E} [\mathbf{a}_t \mathbf{a}_t^\top] - 2 \sum_{t=1}^T \mathbb{E} [\mathbf{a}_t] \boldsymbol{\alpha}^\top + T\boldsymbol{\alpha} \boldsymbol{\alpha}^\top + \boldsymbol{\Psi}_0 \right\} \end{aligned}$$

If we let the prior variance of $\boldsymbol{\alpha}$, σ_α^2 , go to infinity, the MAP of $\boldsymbol{\alpha}$ converges to $\frac{1}{T} \sum_{t=1}^T \mathbb{E} [\mathbf{a}_t]$, which does not depend on \mathbf{G} . In that case, the MAPs of all parameters can be obtained in a single step. In the case of a more informative prior on $\boldsymbol{\alpha}$, we can use the Expectation Conditional Maximization (ECM) approach (Meng and Rubin, 1993) namely by fixing $\boldsymbol{\alpha}$ and updating \mathbf{G} , followed by fixing \mathbf{G} and updating $\boldsymbol{\alpha}$, and continuing iteratively until convergence.

Posterior moments. The posterior quantities required for the M-step thus include $\mathbb{E} [\mathbf{a}_t^\top \mathbf{s}_v]$,

$\mathbb{E}[(\mathbf{a}_t^\top \mathbf{s}_v)^2]$, $\mathbb{E}[\mathbf{a}_t]$, and $\mathbb{E}[\mathbf{a}_t \mathbf{a}_t^\top]$. Since the conditional posteriors of both \mathbf{A} and \mathbf{S} given the other are easy to obtain, we use Gibbs sampling at each iteration to estimate these marginal and joint posterior quantities. The conditional posterior distribution of \mathbf{A} given \mathbf{S} and Θ factorizes across \mathbf{a}_t , $t = 1, \dots, T$. $p(\mathbf{a}_t | \mathbf{Y}, \mathbf{S}, \Theta)$ is Normal with mean and covariance given by

$$\mu(\mathbf{a}_t) = V(\mathbf{a}) \left(\sum_{v=1}^V \frac{1}{\tau_v^2} y_{tv} \mathbf{s}_v + \mathbf{G}^{-1} \boldsymbol{\alpha} \right) \quad \text{and} \quad V(\mathbf{a}_t) \equiv V(\mathbf{a}) = \left(\sum_{v=1}^V \frac{1}{\tau_v^2} \mathbf{s}_v \mathbf{s}_v^\top + \mathbf{G}^{-1} \right)^{-1}.$$

Similarly, the conditional posterior distribution of \mathbf{S} given \mathbf{A} and Θ factorizes across \mathbf{s}_v , $v = 1, \dots, V$. Letting $\mathbf{D}_v = \text{diag}\{\sigma_{qv}^2 : q = 1, \dots, Q\}$, $p(\mathbf{s}_v | \mathbf{Y}, \mathbf{A}, \Theta)$ is Normal with mean and covariance

$$\mu(\mathbf{s}_v) = V(\mathbf{s}_v) \left(\frac{1}{\tau_v^2} \sum_{t=1}^T y_{tv} \mathbf{a}_t + \mathbf{D}_v^{-1} \mathbf{s}_v^0 \right) \quad \text{and} \quad V(\mathbf{s}_v) = \left(\frac{1}{\tau_v^2} \sum_{t=1}^T \mathbf{a}_t \mathbf{a}_t^\top + \mathbf{D}_v^{-1} \right)^{-1}.$$

At each sample from the conditional posterior distribution of \mathbf{A} , for identifiability we rescale the samples to have unit variance across $t = 1, \dots, T$, before proceeding to sample from the conditional posterior distribution of \mathbf{S} . Note that because the conditional posteriors of \mathbf{A} and \mathbf{S} factorize over t and v , respectively, Gibbs sampling can be performed in parallel to facilitate efficient computation. In addition, we avoid matrix inversions when computing $\mu(\mathbf{a}_v)$ and $\mu(\mathbf{s}_v)$ by solving systems of linear equations.

2.2.2 Variational Bayes

While the Gibbs-within-EM approach presented in the previous section is based on well-established Bayesian sampling techniques and EM, the need for sampling at each E-step comes with a high computational cost. VB provides an alternative approach for approximate inference using optimization methods that are computationally efficient. While both the EM-algorithm and VB are examples of the set of variational inference methods, our simulation studies will demonstrate that the VB algorithm described here is computationally advantageous without sacrificing accuracy.

For VB, we assume that the posterior distribution factorizes over \mathbf{S} , \mathbf{A} , \mathbf{G} , $\boldsymbol{\alpha}$, and the noise

variances $\boldsymbol{\tau} = \{\tau_v^2\}_v$. That is, if $\mathbf{Z} = \{\mathbf{S}, \mathbf{A}, \mathbf{G}, \boldsymbol{\alpha}, \boldsymbol{\tau}\}$ represents all the latent variables, we assume that $q(\mathbf{Z}|\mathbf{Y}) = q(\mathbf{S}|\mathbf{Y})q(\mathbf{A}|\mathbf{Y})q(\boldsymbol{\alpha}|\mathbf{Y})q(\mathbf{G}|\mathbf{Y})q(\boldsymbol{\tau}|\mathbf{Y})$. This factorization assumption is fundamental to the VB approach and results in approximate inference. The convergence of the estimators has been studied in various settings, e.g. see Titterton and Wang (2006) for convergence properties of the estimators for a Gaussian mixture model. The approximate posterior for each group of variables is given below. For derivations, see Appendix B.

$q(\mathbf{s}_v|\mathbf{Y})$ is Normal with mean and covariance given by

$$\hat{\mathbf{s}}_v = \hat{V}(\mathbf{s}_v) \left(\frac{1}{\hat{\tau}_v^2} \sum_{t=1}^T y_{tv} \hat{\mathbf{a}}_t + \mathbf{D}_v^{-1} \mathbf{s}_v^0 \right), \quad \hat{V}(\mathbf{s}_v) = \left(\frac{1}{\hat{\tau}_v^2} \sum_{t=1}^T (\hat{\mathbf{a}}_t \hat{\mathbf{a}}_t^\top + \hat{V}(\mathbf{a}_t)) + \mathbf{D}_v^{-1} \right)^{-1}.$$

$q(\mathbf{a}_t|\mathbf{Y})$ is Normal with mean and covariance given by

$$\hat{\mathbf{a}}_t = \hat{V}(\mathbf{a}_t) \left(\sum_{v=1}^V \frac{1}{\hat{\tau}_v^2} y_{tv} \hat{\mathbf{s}}_v + \hat{\mathbf{G}}^{-1} \hat{\boldsymbol{\alpha}} \right), \quad \hat{V}(\mathbf{a}_t) \equiv \hat{V}(\mathbf{a}) = \left(\sum_{v=1}^V \frac{1}{\hat{\tau}_v^2} [\hat{\mathbf{s}}_v \hat{\mathbf{s}}_v^\top + \hat{V}(\mathbf{s}_v)] + \hat{\mathbf{G}}^{-1} \right)^{-1}.$$

$q(\boldsymbol{\alpha}|\mathbf{Y})$ is Normal with mean and covariance, allowing σ_α^2 to be infinity for an uninformative prior, given by

$$\hat{\boldsymbol{\alpha}} = \frac{1}{T} \sum_{t=1}^T \hat{\mathbf{a}}_t, \quad \hat{V}(\boldsymbol{\alpha}) = \hat{\mathbf{G}}/T.$$

$q(\mathbf{G}|\mathbf{Y}) \sim IW(\hat{\boldsymbol{\Psi}}_G, \nu_G)$ with mean $\hat{\mathbf{G}} = (\nu_G - Q - 1)^{-1} \hat{\boldsymbol{\Psi}}_G$, where $\nu_G = \nu_0 + T$ and

$$\hat{\boldsymbol{\Psi}}_G = \boldsymbol{\Psi}_0 + \sum_{t=1}^T (\hat{\mathbf{a}}_t \hat{\mathbf{a}}_t^\top + \hat{V}(\mathbf{a}_t)) - 2\hat{\boldsymbol{\alpha}} \sum_{t=1}^T \hat{\mathbf{a}}_t^\top + T (\hat{\boldsymbol{\alpha}} \hat{\boldsymbol{\alpha}}^\top + \hat{V}(\boldsymbol{\alpha})).$$

$q(\tau_v^2|\mathbf{Y}) \sim IG(\alpha_v, \hat{\beta}_v)$ with mean $\hat{\tau}_v^2 = \frac{\hat{\beta}_v}{\alpha_v - 1}$, where $\alpha_v = \alpha_0 + \frac{T}{2}$ and

$$\hat{\beta}_v = \beta_0 + \frac{1}{2} \sum_{t=1}^T y_{tv}^2 - \left(\sum_{t=1}^T y_{tv} \hat{\mathbf{a}}_t^\top \right) \hat{\mathbf{s}}_v + \frac{1}{2} Tr \left\{ \sum_{t=1}^T (\hat{\mathbf{a}}_t \hat{\mathbf{a}}_t^\top + \hat{V}(\mathbf{a}_t)) (\hat{\mathbf{s}}_v \hat{\mathbf{s}}_v^\top + \hat{V}(\mathbf{s}_v)) \right\}.$$

Note that, comparing with the Gibbs-within-EM algorithm described above, the MAPs for both \mathbf{G} and τ_v^2 have similar forms but with sign differences in the denominator. This is because the MAPs correspond to the modes, rather than to the means, of the IG and IW distributions.

To estimate the posterior moments of each variable, we first use standard template ICA to compute initial estimates for \mathbf{S} , its element-wise variance, and \mathbf{A} , which we use to compute initial estimates for $\boldsymbol{\alpha}$ and \mathbf{G} . We initialize the residual variances τ_v^2 based on the fitted residuals. We then iteratively estimate the approximate posteriors of \mathbf{A} , \mathbf{S} , \mathbf{G} , $\boldsymbol{\alpha}$, and $\boldsymbol{\tau}^2$ until convergence.

3 Simulation Study

We simulate realistic functional MRI data to test the accuracy of the proposed algorithms and compare them with existing approaches. These include our previously proposed template ICA (tICA) model, wherein the temporal mixing matrix is treated as a model parameter rather than a latent variable, and dual regression (DR), an ad-hoc method popular in practice. For each method, we quantify the accuracy of the resulting spatial IC maps and temporal FC matrices, with respect to the unique true subject-level spatial maps and FC matrices. We also assess the sensitivity of each method to the duration of the fMRI time series.

3.1 Data Generation

The generation of subject-specific spatial IC maps is illustrated in Appendix Figure C.1. We set the number of spatial ICs to $Q = 5$ and randomly generate unique subject-level versions of each IC as follows. We first select five real group-average ICs from the Human Connectome Project (HCP) 25-component group ICA (Van Essen et al., 2013) representing three visual network components (IC1, IC2 and IC3), one default mode network (DMN) component (IC4), and one motor network component (IC5). We use these as the basis for the generating mean and set the generating standard deviation (SD) proportional to the mean. For computational convenience, we focus on the left hemisphere and resample (interpolate) to approximately 3000 cortical vertices. To generate a unique subject-level version of each IC, we draw Normal mean-zero samples with the generating standard deviation at each cortical vertex. We then spatially smooth each deviation map using a surface-based Gaussian kernel with 8mm full width at half maximum (FWHM). Smoothing and resampling were performed using the Connectome

Workbench (Marcus et al., 2011) via the ciftiTools R package (Pham et al., 2022). We then add the resulting map, representing the subject-specific deviation, to the generating mean to produce the subject-specific IC maps. An example subject’s deviations and ICs are shown in Appendix Figure C.1. The result is smooth and subtle differences between subjects, a reasonably realistic representation of the differences in functional brain organization that are known to exist between individuals.

We use real fMRI data from the HCP 1200-subject release as the basis for the time courses and functional connectivity used in the simulation. We use the HCP minimally preprocessed, surface-projected fMRI timeseries from the left-to-right (LR) phase encoding direction run of the first visit, containing 1200 volumes (time points). Details of the HCP data processing pipelines can be found in (Glasser et al., 2013). We utilize observations from 1,068 subjects with valid data. To obtain realistic IC timeseries for the simulation study, we first temporally high-pass filter the fMRI data using 10 DCT bases, regress the fMRI data against the 25 HCP group ICs, then select the 5 IC time courses corresponding to the five ICs described above.

Sample IC time courses from 3 example subjects are shown in Appendix Figure C.2, along with their FC matrices, defined as the Pearson correlation between each IC time course. Since within-network connectivity tends to be higher than between-network connectivity, we expect high connectivity within the three visual ICs, and lower connectivity between the visual, DMN and motor ICs. All three subjects show these expected patterns, though individual differences in FC patterns can be clearly seen.

The empirical mean and standard deviation of each FC pair across all 1,068 subjects are shown in Appendix Figure C.3. The mean FC is similar to the patterns seen in the example subjects. The variance patterns show that all FC pairs exhibit variation across subjects, with the weaker connections generally exhibiting the greatest individual differences. To illustrate the effect of our use of the IW distribution for the prior on FC using a setting that mimics the variability observed in this fMRI database, we estimate the IW parameter ν such that the IW variance is no smaller than the empirical variance for any FC pair, as described in Section 2.1. Ψ is then estimated as $\hat{\Psi} = \bar{\mathbf{X}}(\hat{\nu} - Q - 1)$, where $\bar{\mathbf{X}}$ is the empirical mean of FC. The third column of Appendix Figure C.3 shows the standard deviation of each FC pair for the fitted IW

distribution. Note that the IW variance is monotonically related to the magnitude of the mean, unlike our observed FC variance where the opposite phenomenon tends to occur. Therefore, estimating ν such that the empirical variance is not under-estimated for any FC pair leads to a relatively uninformative IW prior for the stronger connections.

The IC time courses are generated in two different ways. In Scenario A, the real time courses described above, plus a small amount of random noise, are used. The goal of this scenario is to be as realistic as possible. In Scenario B, the FC template ICA model is used as the generating model. Specifically, we randomly sample a $T \times T$ covariance matrix Σ from the IW distribution using the parameters estimated as described above. We then randomly sample time courses from a T -dimensional MVN distribution with mean zero and covariance Σ , which we scale to unit variance for identifiability. The goal of this scenario is to provide a benchmark to assess how discrepancies between real fMRI data and the generating model, as in Scenario A, affect the performance of the model. In both scenarios, we let $T = 1200$ (14.4 minutes) to match the HCP data, which has a temporal resolution of 0.72 sec. We also consider the effect of shorter scan duration by varying T from 100 (1.2 minutes) to 800 (9.6 minutes). Note that since FC is known to be dynamic during a scanning session, the ground truth FC of a subject is duration-specific and is defined based on the correlation matrix of the IC time courses for a particular duration.

We use 500 subjects for template estimation and 50 separate subjects to fit the models and evaluate model performance. For each subject, we generate synthetic fMRI data in the following way. Let $\mathbf{E}_{T \times V}$ contain Gaussian white noise with standard deviation σ_e set such that the signal-to-noise ratio (SNR) σ_a/σ_e is equal to 0.5 (Welvaert and Rosseel, 2013), where σ_a^2 is the average variance of IC time courses scaled by the IC spatial intensity at the peak (top 1% of) vertices. This SNR level is chosen to be similar to real fMRI data. The synthetic fMRI data is then given by $\mathbf{Y} = \mathbf{A}\mathbf{S} + \mathbf{E}$, where $\mathbf{S}_{Q \times V}$ contains the Q IC maps and $\mathbf{A}_{T \times Q}$ contains the corresponding IC time courses.

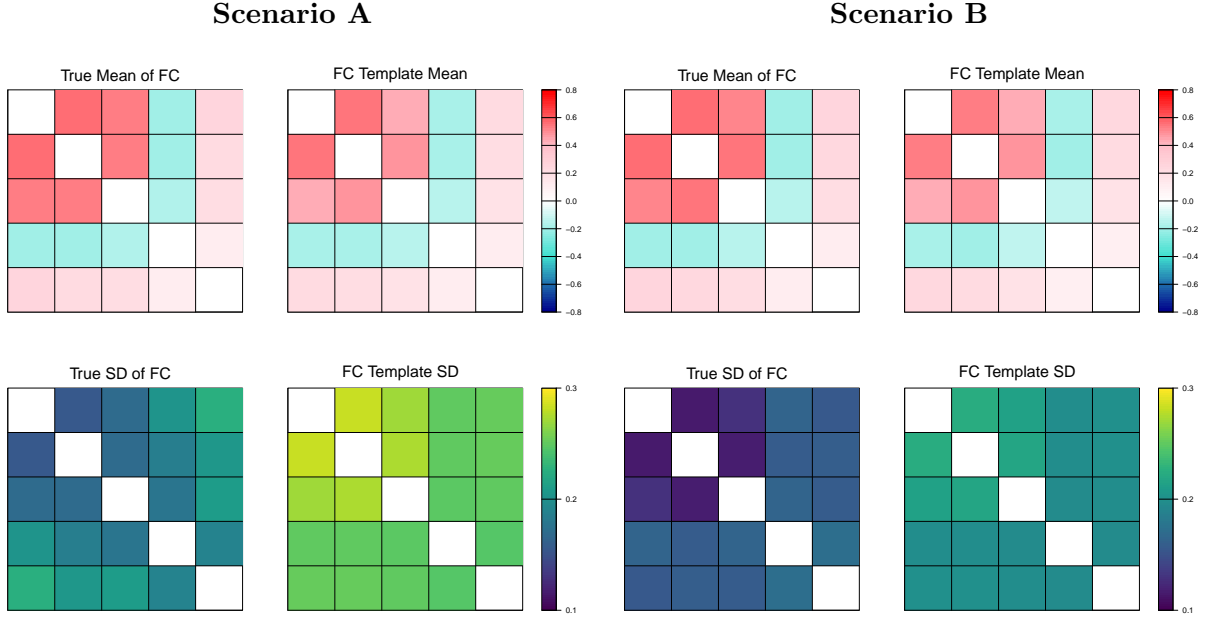


Figure 1: True and IW mean and standard deviation (SD) of functional connectivity (FC). The estimated (template) mean and SD associated with the inverse-Wishart (IW) prior parameters in each scenario, along with the true mean and SD of the subject-level FC matrices. The true FC mean is similar across both scenarios, and the IW (template) mean is a close approximation of the true mean. However, note that the true SD of FC differs across the scenarios, since Scenario A is based on real fMRI time series, while Scenario B is based on draws from the IW distribution. For both scenarios, the IW (template) SD is somewhat higher than the true SD. This is by design to avoid under-estimation of the true SD for any connection, as described in Section 2.1.

3.2 Prior estimation

For each scenario, we estimate the prior parameters for the population priors on the ICs and the FC using the procedure described in Section 2.1, setting the variance inflation factor $\lambda = 0.75$ for a less informative prior on the FC.

Appendix Figures C.4 and C.5 show the estimated prior mean and variance maps for each spatial IC for both simulation scenarios, along with the true (oracle) mean and variance maps. The estimated means are a very close approximation of the true means. The estimated variances closely match the true variances in the high-variance areas but over-estimate the true variance in low-variance areas. This is by design through the biased non-negative variance estimation approach, which seeks to avoid under-estimation of the true variance in favor of a less informative prior.

Figure 1 shows the true mean and variance (SD) of FC, along with the mean and variance

associated with the estimated inverse-Wishart (IW) prior parameters. Across the two simulation scenarios, the FC mean is similar but the true variance differs markedly. Recall that the time series are generated in a different way for each scenario, with Scenario A based on true fMRI time series and Scenario B generated from a multivariate Normal with covariance drawn from an IW distribution. Interestingly, the true variance of FC in Scenario B is lower for stronger connections, similar to the realistic data used in Scenario A but unlike IW-generated covariances whose variance has a monotonic increasing relationship with the magnitude of the mean. This is because FC is based on the time series correlation, the variance of which may not exhibit the same monotonic relationship. In both scenarios, the prior IW variance is higher for stronger connections and is hence over-estimated for most connections, leading to a weaker prior.

3.3 Simulation results

For each of the 50 test subjects, we apply the proposed functional connectivity template ICA (FC-tICA) algorithms (VB and EM), along with two existing methods: standard template ICA (tICA) and the popular ad-hoc method dual regression (DR). For tICA, for maximum comparability we deviate slightly from the original method of Mejia et al. (2020). Specifically, we forego dimension reduction and instead analyze the full $T \times V$ fMRI data, and at each EM iteration we constrain the columns of \mathbf{A} to have unit variance for identifiability. For tICA and FC-tICA, we run each algorithm to a tolerance of 0.001. For the Gibbs-within-EM algorithm for FC-tICA, we run 10 simultaneous Gibbs chains, each consisting of 1000 samples from the joint posterior of \mathbf{A} and \mathbf{S} , and discard the first 50 samples of each chain as burn-in. Here, we summarize the performance of FC-tICA compared with tICA and DR. We utilize the median absolute error (MAE) over 50 test subjects, relative to the subject-specific ground truth measures, as the primary performance metric.

Considering first the spatial IC maps, Supplementary Figure C.6 shows example true and estimated deviation maps for three test subjects for the motor IC (IC 5) for Scenario A. Recall that the spatial ICs for each subject are generated as the prior mean plus a subject-level deviation, as described in Section 3.1. Both standard tICA and the FC-tICA algorithms identify the unique subject-level spatial features. While these features can also be seen in the DR IC estimates,

they exhibit substantially higher noise levels. Supplementary Figures C.7 and C.8 show the accuracy of spatial IC maps in terms of mean absolute error (MAE) for Scenarios A and B, respectively. Similar patterns of accuracy are seen for tICA and FC-tICA, with higher error in areas of engagement and lower error in background areas. As in our prior work comparing tICA with DR (Mejia et al., 2020), the accuracy of DR is much worse than tICA or FC-tICA (results not shown).

Turning to the FC matrices that are our main focus, Figure 2 displays true and estimated functional connectivity (FC) matrices for three different randomly selected test subjects in both scenarios. Unique connectivity features can be seen across the individuals. All methods are able to reveal the unique connectivity features of the individuals reasonably well. Figure 3 summarizes the accuracy of each method across all 50 test subjects. The stronger within-network connections, which are generally of greater interest, are highlighted with a red box on each image. Across all methods and in both scenarios, the weaker connections tend to be more accurately estimated, while the stronger within-network connections tend to exhibit more estimation error. With tICA and FC-tICA, the accuracy of stronger connections is improved. The most accurate within-network connectivity is achieved with FC-tICA using the proposed VB algorithm.

Figure 4 shows the accuracy of FC estimates in Scenario A by scan duration, varying from 200 volumes (~ 2.5 minutes) to 1200 volumes (~ 15 minutes). Supplementary Figure C.9 shows similar trends for Scenario B. Here we only consider the proposed VB algorithm for FC-tICA, since we observe above that it generally outperforms the EM algorithm and is much faster. Since FC is known to vary within a scan, the ground truth FC for each subject is duration-specific, based on the true underlying IC time courses for the duration of the scan. The proposed FC-tICA VB algorithm clearly outperforms tICA and DR, particularly for shorter scan durations.

Figure 5 plots FC estimation error as a function of time series duration for the three within-network connections between the visual ICs. In both simulation scenarios, FC-tICA achieves much smaller error compared with tICA and VB, with the gap between FC-tICA and tICA narrowing somewhat with increased scan duration. Interestingly, DR does not improve visibly with additional scan duration. This may be due to the bias affecting DR specifically, since it

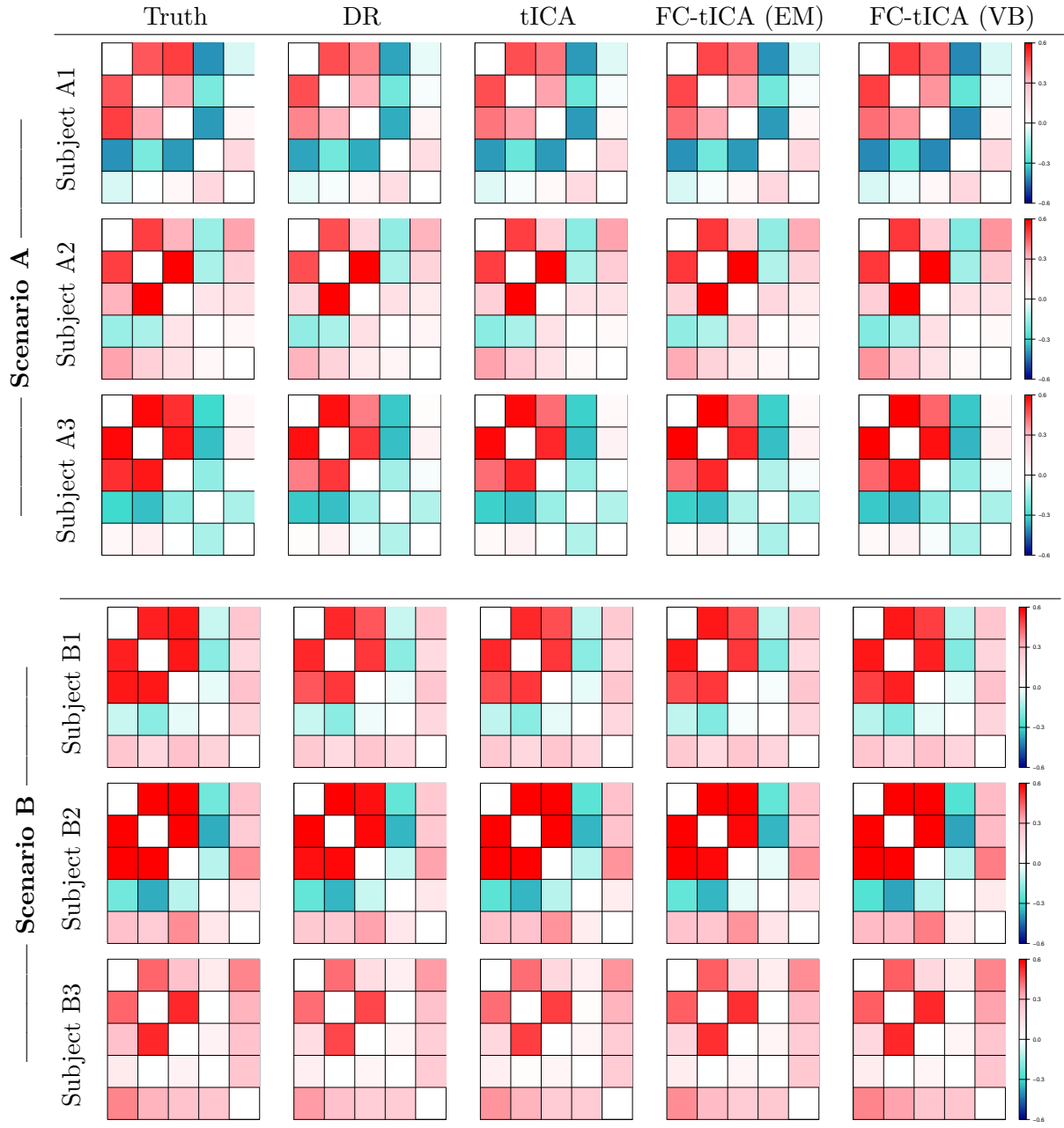


Figure 2: True and estimated subject-level FC matrices in simulation scenarios A and B. In addition to template ICA (tICA) and FC template ICA (FC-tICA), the ad-hoc method dual regression (DR) is displayed for comparison. In three randomly selected test subjects for each scenario, all methods can be seen to capture the unique FC features of each individual reasonably well.

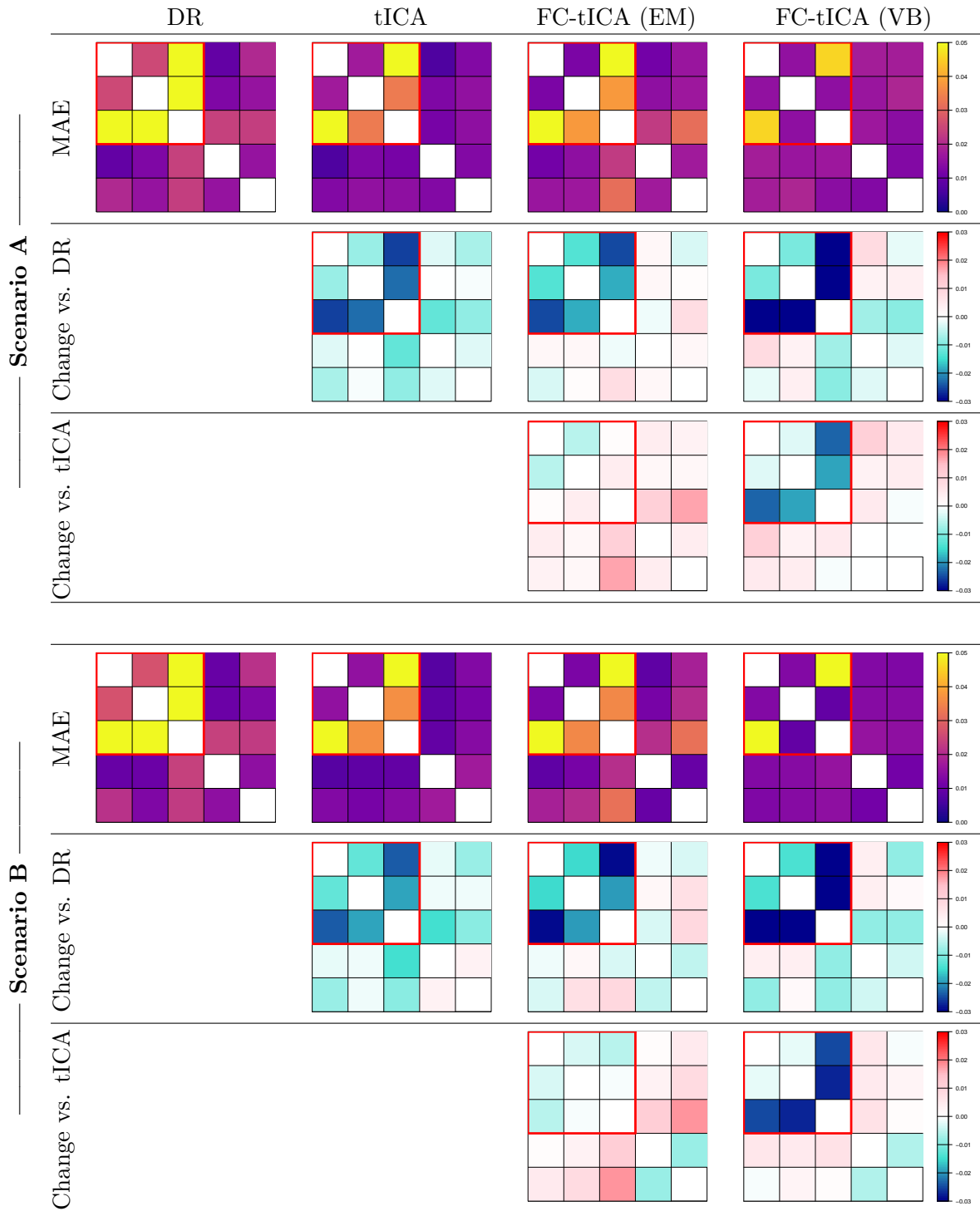


Figure 3: Accuracy of FC estimates across 50 simulated test subjects, in terms of median absolute error (MAE). Also shown are the change in MAE compared with the existing methods dual regression (DR) and template ICA (tICA), where negative values (blue) indicate improved accuracy. The stronger within-network correlations generally of greatest interest are outlined in red. Compared with DR and tICA, the proposed FC template ICA (FC-tICA) algorithms improve accuracy of the stronger correlations. Comparing FC-tICA with tICA, the VB algorithm improves accuracy for the stronger correlations, while worsening some weaker connections of less interest.

uses group-average IC maps as the basis for estimating the temporal activity of each subject-specific IC, a bias that persists regardless of scan duration. Remarkably, FC-tICA based on scan duration of 2.5 min ($T = 200$) (horizontal blue dashed lines) achieves comparable or better accuracy as tICA with 15 minutes of scan time, and much better accuracy than DR with 15 minutes of scan time.

3.4 Computation Time

For the VB algorithm, the average computation time is approximately 1.5 minutes, converging within 12-15 iterations on average with a tolerance of 0.001. Each VB iteration requires less than 1 second on the simulated data, with most of the computation time being related to pre-processing and parameter initialization via tICA. For the Gibbs-within-EM algorithm, the average computation time per subject is approximately 5-6 minutes, converging within 3 EM iterations taking approximately 1 minute each. Compared with standard tICA, the FC-tICA VB algorithm takes almost no additional time, while the Gibbs-within-EM algorithm requires substantially more time due to the Gibbs sampler. Note that in the simulation, the number of vertices $V = 2652$ and the number of ICs $Q = 5$ are much less than typical values in practice. Therefore, we expect the computation time in real data to be much higher, and the computational savings of the VB algorithm versus the Gibbs-within-EM algorithm are likely to be substantial. Since the FC-tICA VB algorithm requires very little computational time over standard tICA, it represents a highly pragmatic model extension.

4 Experimental Data Analysis

4.1 Data Processing and Analysis

We apply the proposed methods and existing methods to resting-state fMRI data from the Human Connectome Project (HCP) 1200-subject release (<http://humanconnectome.org>). The HCP fMRI data were collected on a customized Siemens 3T Skyra scanner with a multiband factor of 8 for high spatial and temporal resolution (Van Essen et al., 2013) and were processed according to the HCP minimal preprocessing pipelines as described in Glasser et al. (2013),

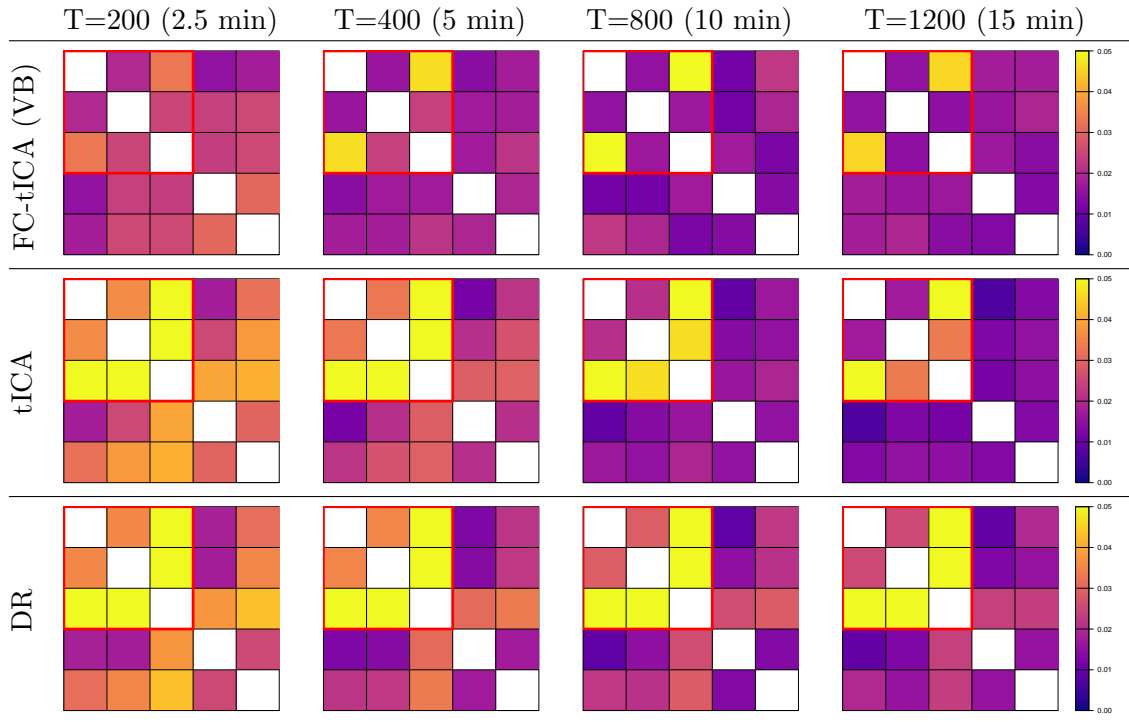


Figure 4: Accuracy of FC estimates by fMRI scan duration in simulation scenario A. Values shown are MAE over 50 test subjects. FC-tICA outperforms existing methods, particularly for shorter durations.

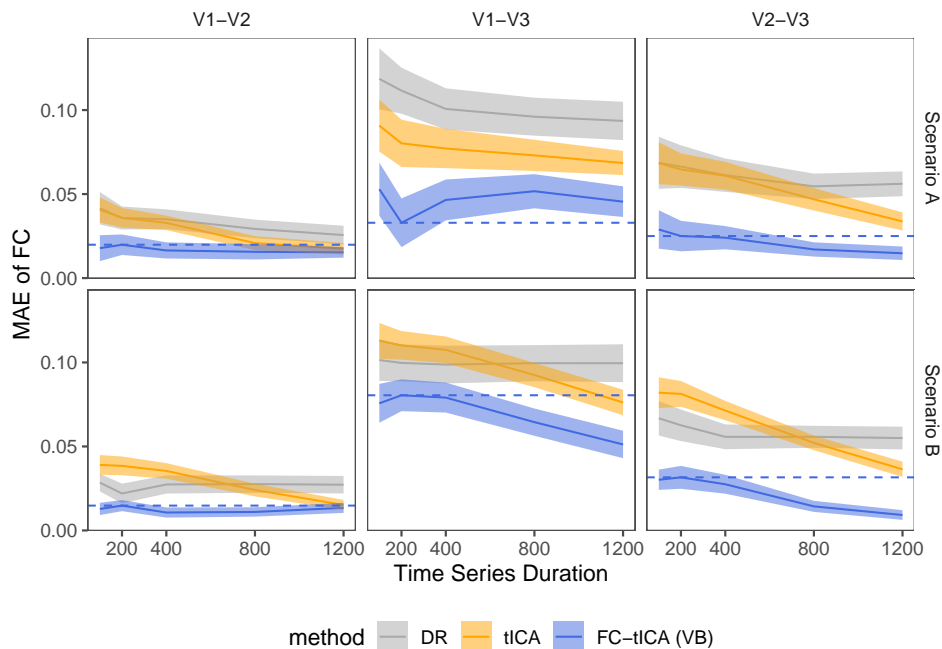


Figure 5: Accuracy of within-network connectivity by fMRI scan duration in simulation study. Each column represents a within-network pair (e.g., V1-V2 indicates the connection between IC 1 and IC 2). Each line shows the median MAE over 50 test subjects; the ribbons show 2 standard errors around the median. Horizontal reference lines show the MAE of FC-tICA with 200 volumes (~ 2.5 min).

including projection to the cortical surface and subcortical parcel segmentation and minimal surface and parcel-constrained smoothing. The final data format is CIFTI grayordinate space, consisting of the left and right cortical surfaces (approximately 32,000 vertices per hemisphere) and the subcortical gray matter structure (approximately 30,000 voxels). We do not perform additional spatial smoothing in order to maximally preserve the functional spatial features of each individual. Each HCP participant underwent four resting-state fMRI runs across two sessions (Smith et al., 2013). The two runs of each session were acquired using opposite phase encoding directions (LR and RL). To avoid spatial differences induced by the different phase encoding directions, here we limit analysis to the LR acquisition. We utilize a version of the fMRI data included in the HCP data release that has been high-pass filtered and denoised via ICA-FIX (Salimi-Khorshidi et al., 2014; Griffanti et al., 2014). We randomly select 362 subjects for template estimation and 100 subjects for analysis, analyzing in total 924 fMRI runs from 462 subjects. For all CIFTI-based analysis, we employ the `ciftiTools` R package (Pham et al., 2022), which requires the Connectome Workbench (Marcus et al., 2011).

Estimation of the prior hyperparameters for FC template ICA and standard template ICA begins with choosing an existing group ICA result or performing group ICA. The HCP 500-subject release includes group ICA results based on nearly 500 subjects at several resolutions, from 25 to 300 components, obtained using Matlab toolbox MELODIC (Beckmann et al., 2005). Here, for a more comprehensive evaluation of the proposed methods we utilize two sets of HCP group ICA results: one at low ($Q = 25$) and one at high ($Q = 100$) resolution. For both ICA resolutions, we estimate the prior hyperparameters for the IC maps and FC based on test-retest data from the 362 training subjects as described in Section 2.1. The prior mean and variance of FC associated with the estimated IW prior, along with the observed empirical mean and variance, are displayed in Figure 6; the prior mean and variance maps for several ICs are displayed in Supplementary Figure D.12. Note that, as by design, the prior variance is generally larger than the empirical variance for FC to avoid an overly informative prior for any FC pair, given the limited flexibility of the IW distribution.

For visualization of the FC matrices, it is common to group ICs by cortical resting-state network (RSN) (e.g. visual, motor) or volumetric region (e.g. cerebellum, basal ganglia). We therefore first assign each IC to a set of established network maps (Yeo et al., 2011) and Freesurfer

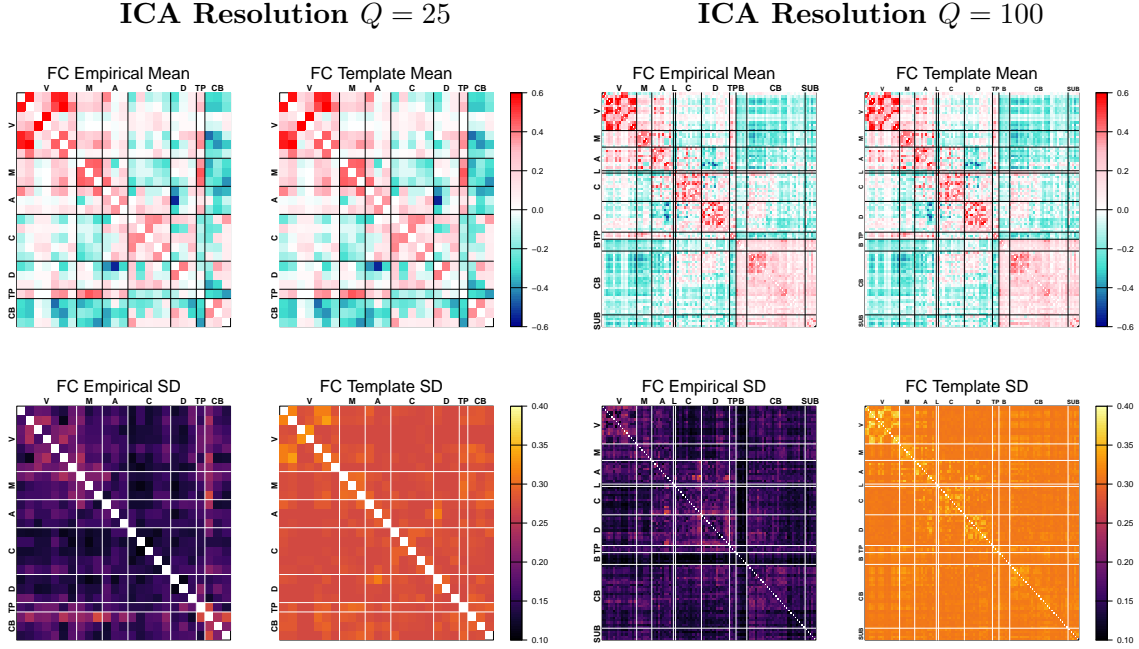


Figure 6: Empirical and inverse-Wishart (IW) prior mean and variance (SD) of functional connectivity (FC) in the HCP analysis. As in the simulation study, note that the prior (“template”) means are similar to the empirical means, while the prior variances tend to be larger than the empirical variances. This is by design to avoid an overly informative prior for any connection, as described in Section 2.1.

subcortical parcels (Fischl, 2012). For this purpose, we first threshold each group ICA map at ± 1 standard deviations from the median for $Q = 25$ and ± 0.5 for $Q = 100$. For each RSN or parcel, we sum up the magnitudes of all overlapping voxels and vertices, then standardize by the square root of the parcel size. Each IC map is then assigned to the RSN or parcel with maximal score. One component scored highest for cerebellum but showed stronger correspondence for a cortical network with second-highest score. To avoid such cases, for ICs assigned to the cerebellum but receiving a runner up score of at least 75% the cerebellar score, we reassign it to the runner up network. We also exclude one IC (IC 74) from the 100-component GICA that appeared to be primarily noise based on visual inspection. Appendix Figures D.10 and D.11 show the thresholded group IC maps and assignments for the 25-component ICA, and Appendix Table D.1 shows the final number of ICs assigned to each network. Appendix Tables D.2 and D.3 report the IC assignments for the 25- and 100-component HCP group ICAs.

We apply FC template ICA (FC-tICA) using the proposed VB algorithm, standard template ICA (tICA), and dual regression (DR) to both sessions for the held-out test subjects. We run

FC-tICA and tICA to a tolerance of 0.001. We use our open-source templateICAr R package (version 7.1) within R version 4.3.1 (R Core Team, 2023) for all analyses. We analyze all $n = 100$ test subjects for the low-resolution ICA ($Q = 25$) to quantify the performance of the proposed methods, while for the high-resolution ICA ($Q = 100$) we analyze a single test subject as a proof of feasibility.

For FC-tICA and tICA, we identify areas of significant “engagement” for each IC by performing a Bayesian hypothesis test at every location using the posterior mean and standard deviation of the spatial IC maps, as described in Mejia et al. (2020). To avoid identifying small effect sizes of little scientific significance, a minimum effect size for the hypothesis tests is set as follows, using a common procedure for thresholding group IC maps: the spatial standard deviation of the prior mean map is computed, and the minimum effect size is set to a multiple of this value. Several examples of the prior mean maps thresholded at twice the standard deviation are displayed in Supplementary Figure D.13, showing that this threshold effectively isolates areas of highest intensity from background areas showing little engagement. In practice, a range of minimum effect sizes can be considered and reported to provide a more comprehensive picture of engagement levels in each individual. We similarly perform hypothesis tests on the subject effects δ_{qv} in equation (2) to identify areas of significant *deviation* from the prior mean for each subject. For these tests, we use a null hypothesis of zero deviation. To correct for multiple comparisons across the brain, we use the Benjamini-Hochberg procedure to control the false discovery rate at 0.05 for each IC map (Benjamini and Hochberg, 1995).

4.2 Results

Figure 7 shows estimated FC matrices for one example test subject at both ICA resolutions. In all cases, the general patterns of stronger within-network connectivity, weaker between-network connectivity, and weaker cortical-subcortical connectivity are seen. FC-tICA and tICA produce quite similar patterns of FC, while the FC patterns seen with DR are somewhat different. This is not unexpected, since dual regression time courses (and hence FC) are based on the group-average IC maps and not the individual-specific IC maps. Therefore, DR-based FC may contain systematic biases driven by individual topographic differences that are not represented

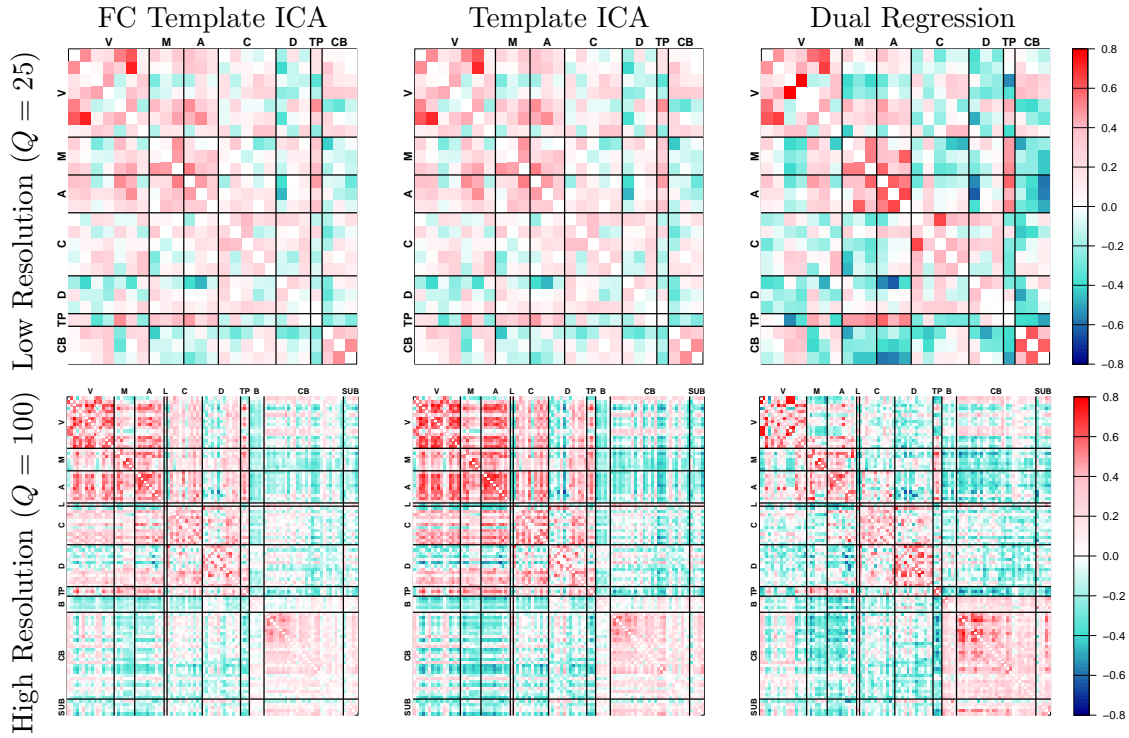


Figure 7: Example FC estimates. For one example subject (100206), FC matrices produced using FC-tICA, tICA and DR are shown for both ICA resolutions. ICs are grouped by network, with abbreviations given in Table D.1. Stronger, positive FC values along the diagonal blocks are indicative of stronger within-network connectivity, as expected. In the high-resolution case, weaker FC values between cortical networks (V to TP) and subcortical regions (BS, CB and SUB) can be seen and are expected.

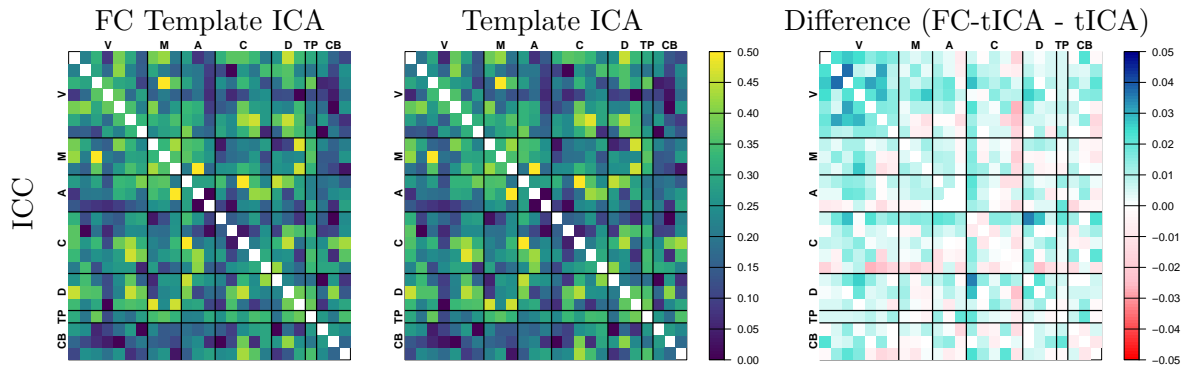


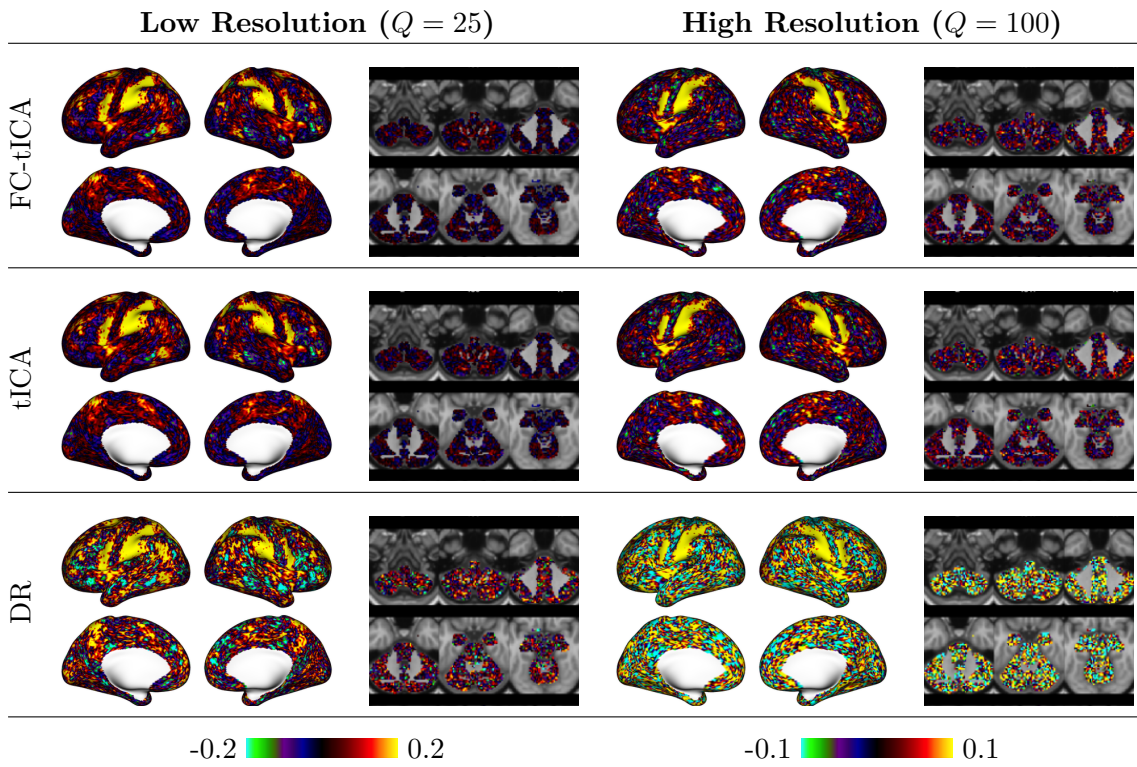
Figure 8: Reliability of FC matrices for low-resolution ICA. Values shown are the intra-class correlation coefficient (ICC), which represents the proportion of variability in the estimates that represents unique subject-level information. The difference between FC-tICA and tICA is shown in the third column. Most FC pairs exhibit improved reliability using FC-tICA. Note that DR is not considered, because the use of group-average ICs to estimate the IC time courses (and hence FC) in dual regression results in inflated reliability metrics due to the presence of systematic biases driven by individual topographic differences.

in group-average IC maps.

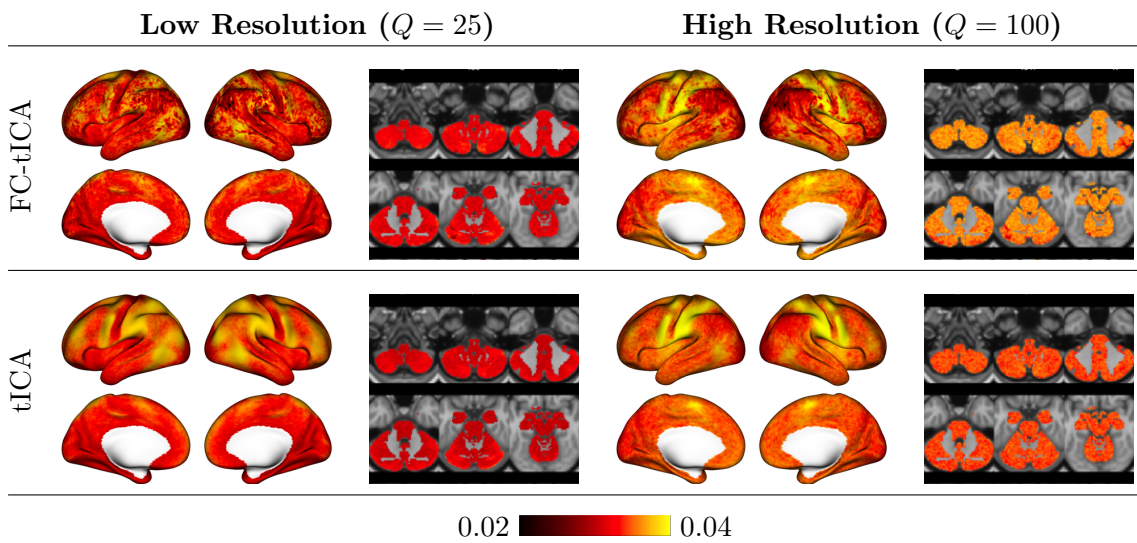
Figure 8 summarizes the reliability of FC in the low-resolution ICA in terms of intra-class correlation coefficient (ICC). Note that while test-retest error measures like MSE or MAE can be spuriously improved due to Bayesian shrinkage towards a group mean, ICC represents the proportion of variance attributable to unique individual features. Thus, higher ICC can be thought to indicate improved estimation of unique subject-level FC features. The ICC of FC-tICA and tICA appears quite similar, but the difference image shows that FC-tICA is higher. This indicates that the FC matrices produced with FC-tICA contain more unique and reliable individual connectivity features versus tICA. Note that DR is not considered here, because the use of group-average ICs to estimate the IC time courses (and hence FC) in dual regression results in inflated reliability metrics due to the presence of systematic (and reliable) biases driven by topographic misalignment.

Figure 9 shows example spatial IC estimates and standard errors for one example IC representing part of the attention network. A similar attention IC appears in the low and high-resolution ICA settings, which allows us to compare the results qualitatively across ICA resolutions. Both FC-tICA and tICA clearly produce much less noisy estimates compared with dual regression (DR). Generally the high-resolution ICs appear noisier than the low-resolution ICs, but this is much worse in the case of DR. This illustrates the powerful noise reduction achieved by FC-tICA and tICA, particularly for higher ICA resolutions where the number of parameters to be estimated increases substantially. Comparing the standard errors across resolutions, they are larger (relative to the scale of the estimates) in the high-resolution ICA, reflecting the increased difficulty in parameter estimation in the high-resolution setting. FC-tICA produces noticeably lower standard errors than tICA, providing more powerful inference.

Figure 10 summarizes the reliability of the spatial IC maps produced with FC-tICA, standard tICA and dual regression, for several example ICs in the low-resolution ICA. Across ICs, both FC-tICA and tICA produce noticeably more reliable IC maps than DR. As expected, FC-tICA and tICA perform similarly in terms of IC estimation, with FC-tICA achieving a slight improvement overall. The average non-background ICC is 0.4052 for FC-tICA versus 0.4037 for standard tICA (0.6% worse on average over ICs), and 0.3606 for DR (11% worse on average



(a) IC Estimates



(b) Standard Errors

Figure 9: Example IC estimates and standard errors. For one example subject (100206), one low-resolution attention IC and one high-resolution attention IC are shown because of their similarity in both resolutions, allowing us to compare results qualitatively across resolutions. Note that standard errors are not produced using dual regression (DR). The template mean and variance for this IC are shown in Supplementary Figure D.12.

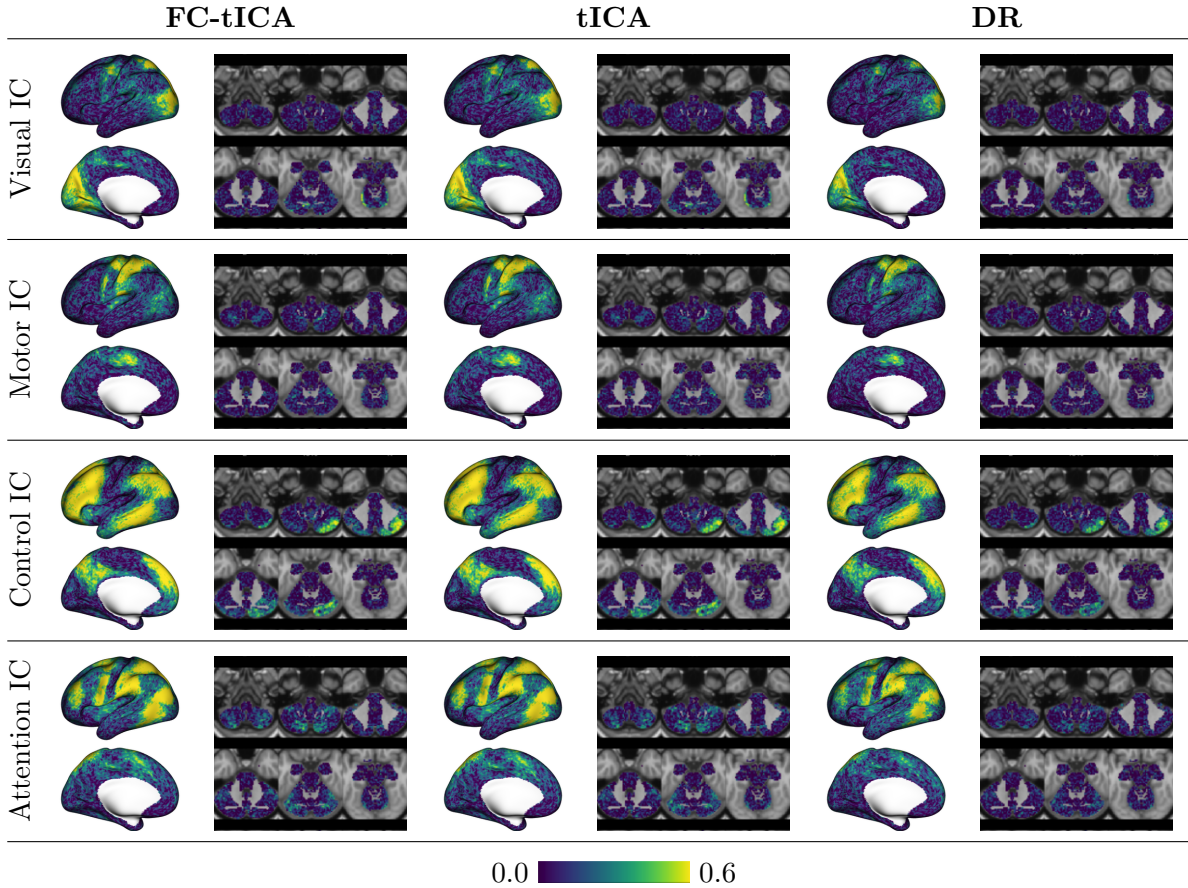


Figure 10: Reliability of spatial IC maps, in terms of intra-class correlation coefficient (ICC), for several example ICs. Only the left hemisphere of the cortex is shown due to space constraints. The ICs shown here are a subset of those shown in Supplementary Figure D.12. Across ICs, ICC tends to be higher within areas of engagement for each IC, which is expected since “background” regions exhibit little between-subject variability. Both FC-tICA and tICA have noticeably higher ICC versus dual regression (DR), particularly in the areas of engagement for each IC. FC-tICA and tICA appear similar, with FC-tICA producing slightly higher ICC on average.

over ICs), where background areas are defined as having prior mean magnitude less than one standard deviation of the template mean map. This shows the significant improvement of both tICA and FC-tICA over DR at estimation of individual spatial topography, reiterating our earlier findings (Mejia et al., 2020). This also shows that FC-tICA does not sacrifice accuracy of IC maps compared with standard tICA and may in fact slightly improve accuracy.

Figure 11 shows example maps of activation and deviation, the results of hypothesis tests described above, for one attention IC in both resolutions. FC-tICA results in somewhat larger areas of activation and deviation versus tICA, likely a reflection of increased power. The size differences across all tests subjects are summarized in Figure 12 below. Comparing the low- and

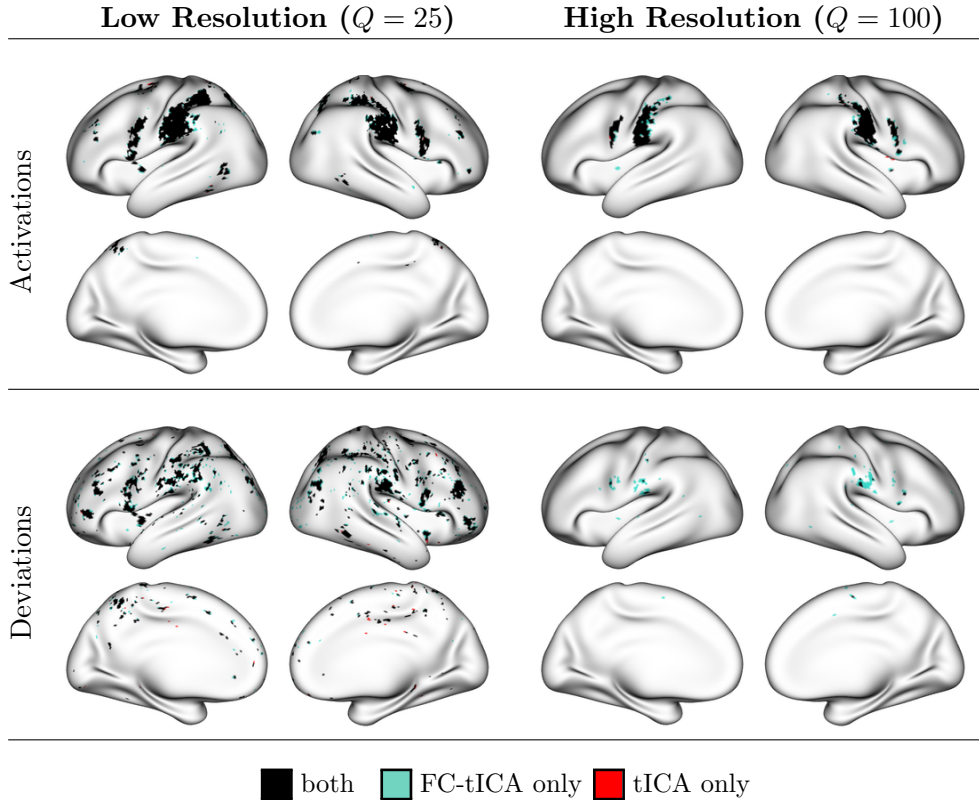


Figure 11: Example areas of activation and deviation. For one example subject (100206), the same low-resolution attention IC and high-resolution attention IC as in Figure 9 are shown. Deviations represent areas where the subject-level IC intensity is significantly higher than the corresponding prior mean intensity. Black regions are those detected with either FC-tICA or tICA; turquoise regions are those detected with FC-tICA only; and red regions are those detected with tICA only. Note that dual regression is not shown because it does not facilitate identifying activations or deviations.

high-resolution ICA settings here, the areas of activation and deviation in the high-resolution ICA are substantially smaller, which is expected given the relatively larger standard errors seen in Figure 11. Note that while the low-resolution attention IC is somewhat more extensive than the high-resolution attention IC based on the prior mean maps (see Supplementary Figure D.13), the difference in the size of activations is much larger, reflecting reduced power to detect effects in the high-resolution setting.

Figure 12 summarizes the size of activations and deviations for each IC when using FC-tICA versus standard tICA. The purple boxplots in the bottom panels show the change in size when using FC-tICA, in terms of the number of brain locations. FC-tICA nearly always results in larger activations and deviations than standard tICA. The median percentage size increase is 11% for activations and 24% for deviations. The larger effect of FC-tICA on the size of

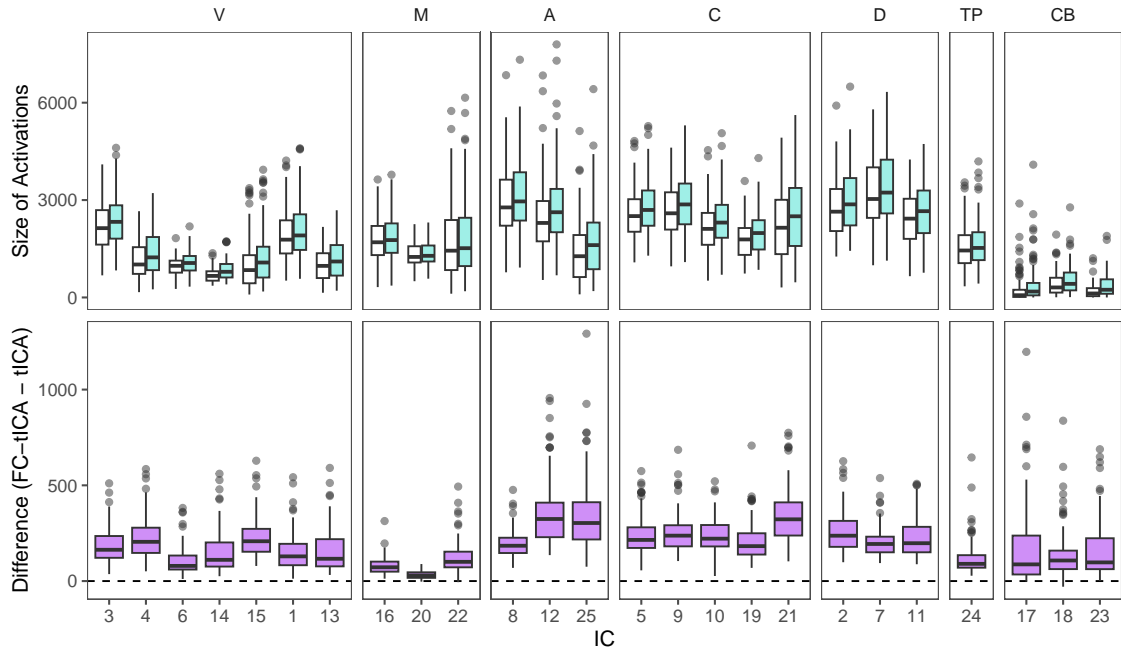
deviations reflects the fact that deviations are generally more difficult to detect than gross activations, as they represent subtle differences between the individual and average patterns of functional topography. The increased power of FC-tICA allows those deviations to be detected with greater sensitivity. Figure 11 shows this even more dramatically for the high-resolution ICA, though in a single subject. This illustrates that the increased power with FC-tICA is most beneficial for harder tasks: that is, identifying deviations, which are more subtle than activations, and identifying significant effects in a high-resolution ICA setting.

4.3 Computation Time

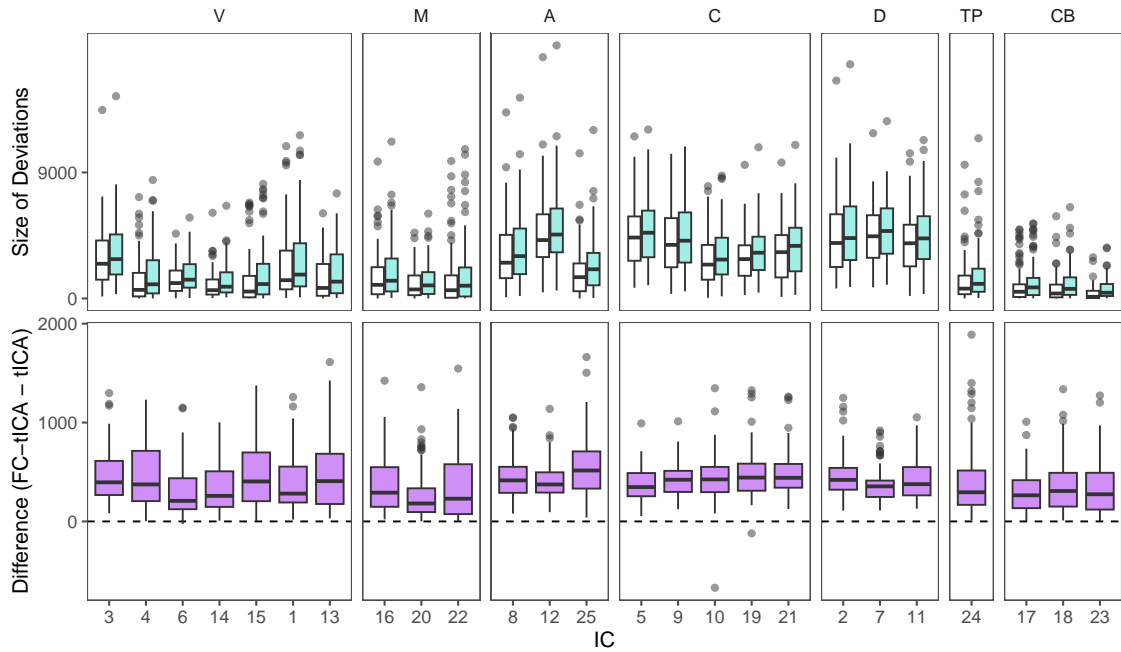
In the low ICA resolution setting, computation time of FC-tICA is approximately 35 minutes per session with scan duration $T = 1200$ and spatial resolution $V = 91,282$, including all preprocessing steps, parameter initialization and model estimation via VB. In the high ICA resolution setting, computation time is approximately 3 hours per session with $T = 1200$ and $V = 59,800$ after resampling each hemisphere to 15,000 vertices to ease the computational burden (note that the $\sim 30,000$ subcortical voxels are not resampled). This approximately halves the number of vertices per hemisphere while retaining a spatial resolution much finer than the spatial features we aim to identify. For additional computational efficiency, we set the number of nuisance ICs to estimate and remove prior to model fitting, as described in Mejia et al. (2020), to 200 for all models.

5 Discussion

In this paper, we have developed a computationally efficient Bayesian independent component analysis method for analysis of functional MRI data. In this model, we employ population-derived priors on both the latent spatial source signals and the temporal activity associated with each source. Through extensive simulation studies and analysis of a large publicly available fMRI dataset, we have shown that the proposed method outperforms two existing methods: a Bayesian ICA model with the temporal activity considered as a parameter rather than a latent variable with a prior distribution, and an ad-hoc method popular in practice for analysis of



(a) Size of Activations



(b) Size of Deviations

Figure 12: Size of activations and deviations with FC-tICA and standard tICA. Units are the total number of cortical vertices and subcortical voxels. Deviations are defined as areas where the subject-level IC intensity is significantly higher than the corresponding prior mean IC intensity. The purple boxplots in the second row represent the increase in size with FC-tICA versus tICA. Boxplots show the distribution across all test subjects by IC, which are grouped by network.

fMRI data. The proposed method is computationally efficient, presenting a realistic alternative to ad-hoc methods, while providing much more accurate estimates of both the spatial and temporal properties of the data, along with powerful inference.

Compared with existing ICA methods, our proposed method has several advantages. First, the algorithm does not require the use of PCA as a preprocessing step and allows for rectangular shapes of the mixing matrix. This reduces the risk of elimination of relevant signals that has been previously observed with PCA followed by ICA (Risk et al., 2019). It also retains the full richness of the temporal signals, necessary for precise estimation of the “functional connectivity” or temporal coordination between spatial sources, often a primary feature of interest in fMRI analysis. Second, an additive noise term is modeled within the algorithm whereas most ICA approaches are based on the noise-free modeling assumption. Third, distributions of the parameter estimates are obtained. This facilitates inference, which is typically not possible via ad-hoc or machine learning-based ICA algorithms. Identifying locations of the brain that are significantly engaged in a particular IC, or identifying significant functional connectivity between ICs, provides a convenient way to summarize ICA results or to extract features for biomarker development.

Besides the clear advantages of noise reduction and ability to perform inference, our proposed method has an additional noteworthy advantage over the popular ad-hoc method dual regression. Dual regression produces temporal activity and functional connectivity in individual subjects based on previously estimated *group-average* IC maps. Misalignment of functional topography between the individual and group averages will induce systematic, reliable bias into functional connectivity estimates. There is growing recognition of this in the fMRI literature. Recent investigations that have found that functional topography of the brain is actually more unique to individuals than functional connectivity, and that many observed individual differences in FC may be driven by individual differences in functional topography that are not accounted for (Bijsterbosch et al., 2018, 2019). Indeed, comparing Figures 10 and 8, we observe higher ICC of spatial topography compared with that of functional connectivity. Along with functional connectivity, functional topography is highly biologically relevant and may be an important source of features for biomarker development in a number of diseases and disorders. It is therefore important to disentangle subject-level functional topography from true functional

connectivity. Our proposed method provides an effective way to achieve this and to produce accurate estimates of both.

This study has several limitations that should be addressed in future work. First, we have not investigated the biological relevance of the features identified by our algorithm. While this is out of the scope of the current investigation, it is an important topic of our ongoing work. Second, our model assumes temporal independence of the residuals, which may not be satisfied in practice. In task fMRI analysis this is often addressed via “prewhitening” or a single iteration of generalized least squares. In ICA the assumption of residual independence is more reasonable versus task fMRI, given that many of the sources of signal and noise are included in the model. Still, it may not be completely satisfied. Third, our model does not account for covariates such as age and sex. Accounting for the influence of relevant covariates at the stage of prior estimation could improve model performance by accounting for some of the between-subject variability and thus reducing the prior variance. We are working to address this in future extensions of the proposed model. Finally, here we have analyzed a single-site study of healthy young adults. Application of the proposed model to more complex datasets, including multi-site datasets requiring harmonization and those focusing on more heterogeneous populations, may require additional nuance and care.

References

- Michal Assaf, Kanchana Jagannathan, Vince D Calhoun, Laura Miller, Michael C Stevens, Robert Sahl, Jacqueline G O’Boyle, Robert T Schultz, and Godfrey D Pearlson. Abnormal functional connectivity of default mode sub-networks in autism spectrum disorder patients. *Neuroimage*, 53(1):247–256, 2010.
- Christian F Beckmann and Stephen M Smith. Probabilistic independent component analysis for functional magnetic resonance imaging. *IEEE transactions on medical imaging*, 23(2):137–152, 2004.
- Christian F Beckmann, Marilena DeLuca, Joseph T Devlin, and Stephen M Smith. Investigations into resting-state connectivity using independent component analysis. *Philosophical*

- Transactions of the Royal Society of London B: Biological Sciences*, 360(1457):1001–1013, 2005.
- Yoav Benjamini and Yosef Hochberg. Controlling the false discovery rate: a practical and powerful approach to multiple testing. *Journal of the Royal Statistical Society: Series B (Statistical Methodology)*, pages 289–300, 1995.
- Janine Diane Bijsterbosch, Mark W Woolrich, Matthew F Glasser, Emma C Robinson, Christian F Beckmann, David C Van Essen, Samuel J Harrison, and Stephen M Smith. The relationship between spatial configuration and functional connectivity of brain regions. *elife*, 7:e32992, 2018.
- Janine Diane Bijsterbosch, Christian F Beckmann, Mark W Woolrich, Stephen M Smith, and Samuel J Harrison. The relationship between spatial configuration and functional connectivity of brain regions revisited. *Elife*, 8:e44890, 2019.
- Rodrigo M Braga and Randy L Buckner. Parallel interdigitated distributed networks within the individual estimated by intrinsic functional connectivity. *Neuron*, 95(2):457–471, 2017.
- Vince D Calhoun, Tulay Adali, Godfrey D Pearlson, and JJ Pekar. A method for making group inferences from functional MRI data using independent component analysis. *Human brain mapping*, 14(3):140–151, 2001.
- BJ Casey, Tariq Cannonier, May I Conley, Alexandra O Cohen, Deanna M Barch, Mary M Heitzeg, Mary E Soules, Theresa Teslovich, Danielle V Dellarco, Hugh Garavan, et al. The adolescent brain cognitive development (ABCD) study: imaging acquisition across 21 sites. *Developmental cognitive neuroscience*, 2018.
- Zaixu Cui, Hongming Li, Cedric H Xia, Bart Larsen, Azeez Adebimpe, Graham L Baum, Matt Cieslak, Raquel E Gur, Ruben C Gur, Tyler M Moore, et al. Individual variation in functional topography of association networks in youth. *Neuron*, 106(2):340–353, 2020.
- Arthur P Dempster, Nan M Laird, and Donald B Rubin. Maximum likelihood from incomplete data via the EM algorithm. *Journal of the Royal Statistical Society: Series B (Methodological)*, 39(1):1–22, 1977.

- Adriana Di Martino, Chao-Gan Yan, Qingyang Li, Erin Denio, Francisco X Castellanos, Kaat Alaerts, Jeffrey S Anderson, Michal Assaf, Susan Y Bookheimer, Mirella Dapretto, et al. The autism brain imaging data exchange: towards a large-scale evaluation of the intrinsic brain architecture in autism. *Molecular psychiatry*, 19(6):659, 2014.
- Ani Eloyan, Ciprian M Crainiceanu, and Brian S Caffo. Likelihood-based population independent component analysis. *Biostatistics*, 14(3):514–527, 2013.
- Seyedeh-Rezvan Farahibozorg, Janine D Bijsterbosch, Weikang Gong, Saad Jbabdi, Stephen M Smith, Samuel J Harrison, and Mark W Woolrich. Hierarchical modelling of functional brain networks in population and individuals from big fMRI data. *NeuroImage*, 243:118513, 2021.
- Bruce Fischl. FreeSurfer. *NeuroImage*, 62(2):774–781, 2012.
- Matthew F Glasser, Stamatios N Sotiropoulos, J Anthony Wilson, Timothy S Coalson, Bruce Fischl, Jesper L Andersson, Junqian Xu, Saad Jbabdi, Matthew Webster, Jonathan R Polimeni, et al. The minimal preprocessing pipelines for the Human Connectome Project. *NeuroImage*, 80:105–124, 2013.
- Evan M Gordon, Timothy O Laumann, Adrian W Gilmore, Dillan J Newbold, Deanna J Greene, Jeffrey J Berg, Mario Ortega, Catherine Hoyt-Drazen, Caterina Gratton, Haoxin Sun, et al. Precision functional mapping of individual human brains. *Neuron*, 95(4):791–807, 2017.
- Michael D Greicius, Gaurav Srivastava, Allan L Reiss, and Vinod Menon. Default-mode network activity distinguishes Alzheimer’s disease from healthy aging: evidence from functional mri. *Proceedings of the National Academy of Sciences*, 101(13):4637–4642, 2004.
- Michael D Greicius, Benjamin H Flores, Vinod Menon, Gary H Glover, Hugh B Solvason, Heather Kenna, Allan L Reiss, and Alan F Schatzberg. Resting-state functional connectivity in major depression: abnormally increased contributions from subgenual cingulate cortex and thalamus. *Biological psychiatry*, 62(5):429–437, 2007.
- Ludovica Griffanti, Gholamreza Salimi-Khorshidi, Christian F Beckmann, Edward J Auerbach, Gwenaëlle Douaud, Claire E Sexton, Enikő Zsoldos, Klaus P Ebmeier, Nicola Filippini, Clare E Mackay, et al. ICA-based artefact removal and accelerated fMRI acquisition for improved resting state network imaging. *Neuroimage*, 95:232–247, 2014.

- Ying Guo and Giuseppe Pagnoni. A unified framework for group independent component analysis for multi-subject fMRI data. *NeuroImage*, 42(3):1078–1093, 2008.
- Ying Guo and Li Tang. A hierarchical model for probabilistic independent component analysis of multi-subject fMRI studies. *Biometrics*, 69(4):970–981, 2013.
- Aapo Hyvarinen, Juha Karhunen, and Erkki Oja. Independent component analysis. *Studies in informatics and control*, 11(2):205–207, 2002.
- Suresh E Joel, Brian S Caffo, Peter CM Van Zijl, and James J Pekar. On the relationship between seed-based and ICA-based measures of functional connectivity. *Magnetic resonance in medicine*, 66(3):644–657, 2011.
- Kevin H Knuth. Bayesian source separation and localization. In *Bayesian Inference for Inverse Problems*, volume 3459, pages 147–158. International Society for Optics and Photonics, 1998.
- Ru Kong, Jingwei Li, Csaba Orban, Mert R Sabuncu, Hesheng Liu, Alexander Schaefer, Nanbo Sun, Xi-Nian Zuo, Avram J Holmes, Simon B Eickhoff, et al. Spatial topography of individual-specific cortical networks predicts human cognition, personality, and emotion. *Cerebral cortex*, 29(6):2533–2551, 2019.
- Timothy O Laumann, Evan M Gordon, Babatunde Adeyemo, Abraham Z Snyder, Sung Jun Joo, Mei-Yen Chen, Adrian W Gilmore, Kathleen B McDermott, Steven M Nelson, Nico UF Dosenbach, et al. Functional system and areal organization of a highly sampled individual human brain. *Neuron*, 87(3):657–670, 2015.
- Neil D Lawrence and Christopher M Bishop. Variational Bayesian independent component analysis. *Univ of Cambridge Tech Report*, 2000.
- Meiling Li, Danhong Wang, Jianxun Ren, Georg Langs, Sophia Stoecklein, Brian P Brennan, Jie Lu, Huafu Chen, and Hesheng Liu. Performing group-level functional image analyses based on homologous functional regions mapped in individuals. *PLoS Biology*, 17(3):e2007032, 2019.
- Shanshan Li, Ani Eloyan, Suresh Joel, Stewart Mostofsky, James Pekar, Susan Spear Bassett, and Brian Caffo. Analysis of group ica-based connectivity measures from fMRI: application to Alzheimer’s disease. *PloS one*, 7(11):e49340, 2012.

- Yu Li, Aiping Liu, Xueyang Fu, Martin J McKeown, Z Jane Wang, and Xun Chen. Atlas-guided parcellation: Individualized functionally-homogenous parcellation in cerebral cortex. *Computers in Biology and Medicine*, 150:106078, 2022.
- Daniel Marcus, John Harwell, Timothy Olsen, Michael Hodge, Matthew Glasser, Fred Prior, Mark Jenkinson, Timothy Laumann, Sandra Curtiss, and David Van Essen. Informatics and data mining tools and strategies for the Human Connectome Project. *Frontiers in Neuroinformatics*, 5:4, 2011.
- Martin J McKeown, Scott Makeig, Greg G Brown, Tzyy-Ping Jung, Sandra S Kindermann, Anthony J Bell, and Terrence J Sejnowski. Analysis of fMRI data by blind separation into independent spatial components. *Human brain mapping*, 6(3):160–188, 1998.
- Amanda F Mejia, Mary Beth Nebel, Yikai Wang, Brian S Caffo, and Ying Guo. Template independent component analysis: Targeted and reliable estimation of subject-level brain networks using big data population priors. *Journal of the American Statistical Association*, 115(531):1151–1177, 2020.
- Xiao-Li Meng and Donald B Rubin. Maximum likelihood estimation via the ecm algorithm: A general framework. *Biometrika*, 80(2):267–278, 1993.
- Ali Mohammad-Djafari. A Bayesian approach to source separation. In *AIP Conference proceedings*, volume 567, pages 221–244. American Institute of Physics, 2001.
- Susanne G Mueller, Michael W Weiner, Leon J Thal, Ronald C Petersen, Clifford Jack, William Jagust, John Q Trojanowski, Arthur W Toga, and Laurel Beckett. The Alzheimer’s Disease Neuroimaging Initiative. *Neuroimaging Clinics*, 15(4):869–877, 2005.
- Mary Beth Nebel, Ani Eloyan, Anita D Barber, and Stewart H Mostofsky. Precentral gyrus functional connectivity signatures of autism. *Frontiers in systems neuroscience*, 8:80, 2014.
- Steven W Nydick. The wishart and inverse wishart distributions. *Electronic Journal of Statistics*, 6(1-19), 2012.
- Damon D Pham, John Muschelli, and Amanda F Mejia. ciftiTools: A package for reading, writing, visualizing, and manipulating CIFTI files in R. *NeuroImage*, 250:118877, 2022.

- R Core Team. *R: A Language and Environment for Statistical Computing*. R Foundation for Statistical Computing, Vienna, Austria, 2023. URL <https://www.R-project.org/>.
- Benjamin B Risk, David S Matteson, and David Ruppert. Linear non-Gaussian component analysis via maximum likelihood. *Journal of the American Statistical Association*, 114(525): 332–343, 2019.
- Gholamreza Salimi-Khorshidi, Gwenaëlle Douaud, Christian F Beckmann, Matthew F Glasser, Ludovica Griffanti, and Stephen M Smith. Automatic denoising of functional MRI data: combining independent component analysis and hierarchical fusion of classifiers. *Neuroimage*, 90:449–468, 2014.
- Alexander Schaefer, Ru Kong, Evan M Gordon, Timothy O Laumann, Xi-Nian Zuo, Avram J Holmes, Simon B Eickhoff, and BT Thomas Yeo. Local-global parcellation of the human cerebral cortex from intrinsic functional connectivity MRI. *Cerebral cortex*, 28(9):3095–3114, 2018.
- Stephen M Smith, Christian F Beckmann, Jesper Andersson, Edward J Auerbach, Janine Bijnsterbosch, Gwenaëlle Douaud, Eugene Duff, David A Feinberg, Ludovica Griffanti, Michael P Harms, et al. Resting-state fMRI in the Human Connectome Project. *Neuroimage*, 80:144–168, 2013.
- Cathie Sudlow, John Gallacher, Naomi Allen, Valerie Beral, Paul Burton, John Danesh, Paul Downey, Paul Elliott, Jane Green, Martin Landray, et al. UK Biobank: an open access resource for identifying the causes of a wide range of complex diseases of middle and old age. *PLoS medicine*, 12(3):e1001779, 2015.
- DM Titterington and Bo Wang. Convergence properties of a general algorithm for calculating variational bayesian estimates for a normal mixture model. 2006.
- Nathalie Tzourio-Mazoyer, Brigitte Landeau, Dimitri Papathanassiou, Fabrice Crivello, Octave Etard, Nicolas Delcroix, Bernard Mazoyer, and Marc Joliot. Automated anatomical labeling of activations in SPM using a macroscopic anatomical parcellation of the MNI MRI single-subject brain. *Neuroimage*, 15(1):273–289, 2002.

Vincent G van de Ven, Elia Formisano, David Prvulovic, Christian H Roeder, and David EJ Linden. Functional connectivity as revealed by spatial independent component analysis of fMRI measurements during rest. *Human brain mapping*, 22(3):165–178, 2004.

David C Van Essen, Stephen M Smith, Deanna M Barch, Timothy EJ Behrens, Essa Yacoub, Kamil Ugurbil, WU-Minn HCP Consortium, et al. The WU-Minn Human Connectome Project: An overview. *NeuroImage*, 80:62–79, 2013.

Marijke Welvaert and Yves Rosseel. On the definition of signal-to-noise ratio and contrast-to-noise ratio for fmri data. *PloS one*, 8(11):e77089, 2013.

BT Thomas Yeo, Fenna M Krienen, Jorge Sepulcre, Mert R Sabuncu, Danial Lashkari, Marisa Hollinshead, Joshua L Roffman, Jordan W Smoller, Lilla Zöllei, Jonathan R Polimeni, et al. The organization of the human cerebral cortex estimated by intrinsic functional connectivity. *Journal of neurophysiology*, 2011.

A EM Derivation

The log-posterior for the parameters Θ , given the latent variables \mathbf{S} and \mathbf{A} , is

$$\begin{aligned}
\log p(\Theta|\mathbf{Y}, \mathbf{S}, \mathbf{A}) &\propto \log \{p(\mathbf{Y}|\mathbf{A}, \mathbf{S}, \Theta)p(\mathbf{S})p(\mathbf{A}|\Theta)p(\Theta)\} \\
&= \log p(\mathbf{Y}|\mathbf{A}, \mathbf{S}, \Theta) + \log p(\mathbf{S}) + \log p(\mathbf{A}|\Theta) + \log p(\Theta) \\
&= \sum_{v=1}^V \sum_{t=1}^T \log p(y_{tv}|\mathbf{a}_t, \mathbf{s}_v, \tau_v^2) + \sum_{v=1}^V \sum_{q=1}^Q \log p(s_{qv}) + \sum_{t=1}^T \log p(\mathbf{a}_t|\boldsymbol{\alpha}, \mathbf{G}) \\
&\quad + \log p(\mathbf{G}) + \log p(\boldsymbol{\alpha}) + \sum_{v=1}^V \log p(\tau_v^2) \\
&= \sum_{v=1}^V \sum_{t=1}^T \log g(y_{tv} : \mathbf{a}_t^\top \mathbf{s}_v, \tau_v^2) + \sum_{v=1}^V \sum_{q=1}^Q \log g(s_{qv} : s_{qv}^0, \sigma_{qv}^2) + \sum_{t=1}^T \log g(\mathbf{a}_t : \boldsymbol{\alpha}, \mathbf{G}) \\
&\quad + \log f_{IW}(\mathbf{G} : \boldsymbol{\Psi}_0, \nu_0) + \sum_{q=1}^Q \log g(\boldsymbol{\alpha} : \mathbf{0}, \sigma_\alpha^2 \mathbf{I}) + \sum_{v=1}^V \log f_{IG}(\tau_v^2 : \alpha_0, \beta_0),
\end{aligned}$$

where $g(\cdot : \boldsymbol{\mu}, \boldsymbol{\Sigma})$ denotes the Gaussian density, $f_{IW}(\cdot : \boldsymbol{\Psi}, \nu)$ denotes the IW density, and $f_{IG}(\cdot : \alpha, \beta)$ denotes the IG density.

E-step: The expected value of the log-posterior of the parameters given their values in the previous iteration step is defined as follows.

$$Q(\Theta|\hat{\Theta}^{(k)}) = \mathbb{E} [p(\Theta|\mathbf{Y}, \mathbf{S}, \mathbf{A})] \propto Q_1(\Theta|\hat{\Theta}^{(k)}) + Q_2(\Theta|\hat{\Theta}^{(k)}),$$

where $Q_1(\Theta|\hat{\Theta}^{(k)})$ contains the terms involving τ_v^2 and $Q_2(\Theta|\hat{\Theta}^{(k)})$ contains the terms involving $\boldsymbol{\alpha}$ and \mathbf{G} . Each expectation below is over the conditional posterior of (\mathbf{S}, \mathbf{A}) , given the current parameter estimates $\hat{\Theta}^{(k)}$ at iteration k .

$$\begin{aligned}
Q_1(\Theta|\hat{\Theta}^{(k)}) &= \sum_{v=1}^V \sum_{t=1}^T \mathbb{E} [\log p(y_{tv}|\mathbf{a}_t, \mathbf{s}_v, \tau_v^2)] + \sum_{v=1}^V \log p(\tau_v^2) \\
&= \sum_{v=1}^V \sum_{t=1}^T \mathbb{E} \left[\log \left\{ \frac{1}{\sqrt{2\pi\tau_v^2}} \exp \left(-\frac{1}{2\tau_v^2} (y_{tv} - \mathbf{a}_t^\top \mathbf{s}_v)^2 \right) \right\} \right] \\
&\quad + \sum_{v=1}^V \log \left\{ \frac{\beta_0^{\alpha_0}}{\Gamma(\alpha_0)} (\tau_v^2)^{-(\alpha_0+1)} \exp \left(-\frac{\beta_0}{\tau_v^2} \right) \right\}
\end{aligned}$$

$$\begin{aligned}
& \propto -\frac{T}{2} \sum_{v=1}^V \log(\tau_v^2) - \sum_{v=1}^V \frac{1}{2\tau_v^2} \sum_{t=1}^T \left\{ y_{tv}^2 - 2y_{tv} \mathbb{E} \left[\mathbf{a}_t^\top \mathbf{s}_v \right] + \mathbb{E} \left[(\mathbf{a}_t^\top \mathbf{s}_v)^2 \right] \right\} \\
& - (\alpha_0 + 1) \sum_{v=1}^V \log(\tau_v^2) - \beta_0 \sum_{v=1}^V \frac{1}{\tau_v^2}
\end{aligned}$$

and

$$\begin{aligned}
Q_2(\Theta | \hat{\Theta}^{(k)}) &= \sum_{t=1}^T \mathbb{E} [\log p(\mathbf{a}_t | \boldsymbol{\alpha}, \mathbf{G})] + \log p(\mathbf{G}) + \log p(\boldsymbol{\alpha}) \\
&\propto -T \log |\mathbf{G}| - \sum_{t=1}^T \mathbb{E} \left[(\mathbf{a}_t - \boldsymbol{\alpha})^\top \mathbf{G}^{-1} (\mathbf{a}_t - \boldsymbol{\alpha}) \right] \\
&\quad - (\nu_0 + Q + 1) \log |\mathbf{G}| - \text{Tr} \{ \boldsymbol{\Psi}_0 \mathbf{G}^{-1} \} - \frac{\boldsymbol{\alpha}^\top \boldsymbol{\alpha}}{\sigma_\alpha^2} \\
&= -\text{Tr} \left\{ \mathbf{G}^{-1} \sum_{t=1}^T \mathbb{E} \left[\mathbf{a}_t \mathbf{a}_t^\top \right] \right\} + 2\boldsymbol{\alpha}^\top \mathbf{G}^{-1} \sum_{t=1}^T \mathbb{E} [\mathbf{a}_t] - T\boldsymbol{\alpha}^\top \mathbf{G}^{-1} \boldsymbol{\alpha} \\
&\quad - (T + \nu_0 + Q + 1) \log |\mathbf{G}| - \text{Tr} \{ \boldsymbol{\Psi}_0 \mathbf{G}^{-1} \} - \frac{\boldsymbol{\alpha}^\top \boldsymbol{\alpha}}{\sigma_\alpha^2}
\end{aligned}$$

Posterior moments. The conditional posterior distribution of \mathbf{A} given \mathbf{S} and Θ factorizes across \mathbf{a}_t , $t = 1, \dots, T$, and is given by

$$\begin{aligned}
p(\mathbf{a}_t | \mathbf{Y}, \mathbf{S}, \Theta) &\propto \prod_{v=1}^V p(y_{tv} | \mathbf{a}_t, \mathbf{s}_v, \Theta) p(\mathbf{a}_t | \Theta) \\
&\propto \exp \left\{ -\frac{1}{2} \sum_{v=1}^V \frac{1}{\tau_v^2} (y_{tv} - \mathbf{a}_t^\top \mathbf{s}_v)^2 \right\} \exp \left\{ -\frac{1}{2} (\mathbf{a}_t - \boldsymbol{\alpha})^\top \mathbf{G}^{-1} (\mathbf{a}_t - \boldsymbol{\alpha}) \right\} \\
&\propto \exp \left\{ -\frac{1}{2} \left[\mathbf{a}_t^\top \left(\sum_{v=1}^V \frac{1}{\tau_v^2} \mathbf{s}_v \mathbf{s}_v^\top + \mathbf{G}^{-1} \right) \mathbf{a}_t - 2\mathbf{a}_t^\top \left(\sum_{v=1}^V \frac{1}{\tau_v^2} y_{tv} \mathbf{s}_v + \mathbf{G}^{-1} \boldsymbol{\alpha} \right) \right] \right\}.
\end{aligned}$$

Hence, $p(\mathbf{a}_t | \mathbf{Y}, \mathbf{S}, \Theta)$ is Normal with mean and covariance given by

$$\mu(\mathbf{a}_t) = V(\mathbf{a}) \left(\sum_{v=1}^V \frac{1}{\tau_v^2} y_{tv} \mathbf{s}_v + \mathbf{G}^{-1} \boldsymbol{\alpha} \right) \quad \text{and} \quad V(\mathbf{a}_t) \equiv V(\mathbf{a}) = \left(\sum_{v=1}^V \frac{1}{\tau_v^2} \mathbf{s}_v \mathbf{s}_v^\top + \mathbf{G}^{-1} \right)^{-1}.$$

Similarly, the conditional posterior distribution of \mathbf{S} given \mathbf{A} and Θ factorizes across \mathbf{s}_v ,

$v = 1, \dots, V$. Letting $\mathbf{D}_v = \text{diag}\{\sigma_{qv}^2 : q = 1, \dots, Q\}$, it is given by

$$\begin{aligned} p(\mathbf{s}_v | \mathbf{Y}, \mathbf{A}, \Theta) &\propto \prod_{t=1}^T p(y_{tv} | \mathbf{a}_t, \mathbf{s}_v, \Theta) p(\mathbf{s}_v | \Theta) \\ &\propto \exp \left\{ -\frac{1}{2\tau_v^2} \sum_{t=1}^T (y_{tv} - \mathbf{a}_t^\top \mathbf{s}_v)^2 \right\} \exp \left\{ -\frac{1}{2} (\mathbf{s}_v - \mathbf{s}_v^0)^\top \mathbf{D}_v^{-1} (\mathbf{s}_v - \mathbf{s}_v^0) \right\} \\ &\propto \exp \left\{ -\frac{1}{2} \left[\mathbf{s}_v^\top \left(\frac{1}{\tau_v^2} \sum_{t=1}^T \mathbf{a}_t \mathbf{a}_t^\top + \mathbf{D}_v^{-1} \right) \mathbf{s}_v - 2\mathbf{s}_v^\top \left(\frac{1}{\tau_v^2} \sum_{t=1}^T y_{tv} \mathbf{a}_t + \mathbf{D}_v^{-1} \mathbf{s}_v^0 \right) \right] \right\}. \end{aligned}$$

Hence, $p(\mathbf{s}_v | \mathbf{Y}, \mathbf{A}, \Theta)$ is Normal with mean and covariance

$$\mu(\mathbf{s}_v) = V(\mathbf{s}_v) \left(\frac{1}{\tau_v^2} \sum_{t=1}^T y_{tv} \mathbf{a}_t + \mathbf{D}_v^{-1} \mathbf{s}_v^0 \right) \quad \text{and} \quad V(\mathbf{s}_v) = \left(\frac{1}{\tau_v^2} \sum_{t=1}^T \mathbf{a}_t \mathbf{a}_t^\top + \mathbf{D}_v^{-1} \right)^{-1}.$$

B VB Derivation

B.1 Approximate posterior of \mathbf{S}

Beginning with \mathbf{S} , the full conditional posterior factorizes over locations $v = 1, \dots, V$. For \mathbf{s}_v , letting $\mathbf{D}_v = \text{diag}\{\sigma_{qv}^2 : q = 1, \dots, Q\}$, the approximate log posterior is given by

$$\begin{aligned} \log q(\mathbf{s}_v | \mathbf{Y}) &= \mathbb{E}_{\mathbf{A}, \tau_v^2} [\log p(\mathbf{y}_{\cdot, v} | \mathbf{A}, \mathbf{s}_v, \tau_v^2) + \log p(\mathbf{s}_v)] + \text{const} \\ &\propto -\frac{1}{2} \mathbb{E}_{\mathbf{A}, \tau_v^2} \left[\sum_{t=1}^T \frac{1}{\tau_v^2} (y_{tv} - \mathbf{a}_t^\top \mathbf{s}_v)^2 \right] + (\mathbf{s}_v - \mathbf{s}_v^0)^\top \mathbf{D}_v^{-1} (\mathbf{s}_v - \mathbf{s}_v^0) \\ &\propto -\frac{1}{2} \mathbb{E}_{\mathbf{A}, \tau_v^2} \left[\frac{1}{\tau_v^2} \left\{ -2\mathbf{s}_v^\top \left(\sum_{t=1}^T y_{tv} \mathbf{a}_t \right) + \mathbf{s}_v^\top \left(\sum_{t=1}^T \mathbf{a}_t \mathbf{a}_t^\top \right) \mathbf{s}_v \right\} + \mathbf{s}_v^\top \mathbf{D}_v^{-1} \mathbf{s}_v - 2\mathbf{s}_v^\top \mathbf{D}_v^{-1} \mathbf{s}_v^0 \right] \\ &= -\frac{1}{2} \left\{ -2\mathbf{s}_v^\top \left(\frac{1}{\hat{\tau}_v^2} \sum_{t=1}^T y_{tv} \hat{\mathbf{a}}_t + \mathbf{D}_v^{-1} \mathbf{s}_v^0 \right) + \mathbf{s}_v^\top \left(\frac{1}{\hat{\tau}_v^2} \sum_{t=1}^T (\hat{\mathbf{a}}_t \hat{\mathbf{a}}_t^\top + \hat{V}(\mathbf{a}_t)) + \mathbf{D}_v^{-1} \right) \mathbf{s}_v \right\} \end{aligned}$$

where $\hat{\tau}_v^2$ is the approximate posterior mean of τ_v^2 based on $q(\tau_v^2 | \mathbf{Y})$, and $\hat{\mathbf{a}}_t$ and $\hat{V}(\mathbf{a}_t)$ are the approximate posterior mean and covariance of \mathbf{a}_t based on $q(\mathbf{A} | \mathbf{Y})$. Hence, $q(\mathbf{s}_v | \mathbf{Y})$ is Normal with mean and covariance given by

$$\hat{\mathbf{s}}_v = \hat{V}(\mathbf{s}_v) \left(\frac{1}{\hat{\tau}_v^2} \sum_{t=1}^T y_{tv} \hat{\mathbf{a}}_t + \mathbf{D}_v^{-1} \mathbf{s}_v^0 \right) \quad (6)$$

$$\hat{V}(\mathbf{s}_v) = \left(\frac{1}{\hat{\tau}_v^2} \sum_{t=1}^T \left(\hat{\mathbf{a}}_t \hat{\mathbf{a}}_t^\top + \hat{V}(\mathbf{a}_t) \right) + \mathbf{D}_v^{-1} \right)^{-1}. \quad (7)$$

B.2 Approximate posterior of \mathbf{A}

Turning to \mathbf{A} , the full conditional posterior factorizes over time points $t = 1, \dots, T$, and the approximate log posterior for \mathbf{a}_t is given by

$$\begin{aligned} \log q(\mathbf{a}_t | \mathbf{Y}) &= \mathbb{E}_{\mathbf{S}, \mathbf{G}, \boldsymbol{\alpha}, \boldsymbol{\tau}} [\log p(\mathbf{y}_t | \mathbf{a}_t, \mathbf{S}, \boldsymbol{\tau}) + \log p(\mathbf{a}_t | \boldsymbol{\alpha}, \mathbf{G})] + \text{const} \\ &\propto -\frac{1}{2} \mathbb{E}_{\mathbf{S}, \mathbf{G}, \boldsymbol{\alpha}, \boldsymbol{\tau}} \left[\sum_{v=1}^V \frac{1}{\hat{\tau}_v^2} (y_{tv} - \mathbf{s}_v^\top \mathbf{a}_t)^2 + (\mathbf{a}_t - \boldsymbol{\alpha})^\top \mathbf{G}^{-1} (\mathbf{a}_t - \boldsymbol{\alpha}) \right] \\ &\propto -\frac{1}{2} \mathbb{E}_{\mathbf{S}, \mathbf{G}, \boldsymbol{\alpha}, \boldsymbol{\tau}} \left[-2\mathbf{a}_t^\top \left(\sum_{v=1}^V \frac{1}{\hat{\tau}_v^2} y_{tv} \mathbf{s}_v + \mathbf{G}^{-1} \boldsymbol{\alpha} \right) + \mathbf{a}_t^\top \left(\sum_{v=1}^V \frac{1}{\hat{\tau}_v^2} \mathbf{s}_v \mathbf{s}_v^\top + \mathbf{G}^{-1} \right) \mathbf{a}_t \right] \\ &= -\frac{1}{2} \left\{ -2\mathbf{a}_t^\top \left(\sum_{v=1}^V \frac{1}{\hat{\tau}_v^2} y_{tv} \hat{\mathbf{s}}_v + \hat{\mathbf{G}}^{-1} \hat{\boldsymbol{\alpha}} \right) + \mathbf{a}_t^\top \left(\sum_{v=1}^V \frac{1}{\hat{\tau}_v^2} [\hat{\mathbf{s}}_v \hat{\mathbf{s}}_v^\top + \hat{V}(\mathbf{s}_v)] + \hat{\mathbf{G}}^{-1} \right) \mathbf{a}_t \right\}, \end{aligned}$$

where $\hat{\boldsymbol{\alpha}}$ and $\hat{\mathbf{G}}$ are the approximate posterior means of $\boldsymbol{\alpha}$ and \mathbf{G} , respectively, and $\hat{\mathbf{s}}_v$ and $\hat{V}(\mathbf{s}_v)$ are the approximate posterior mean and covariance of \mathbf{s}_v , given above. Then $q(\mathbf{a}_t | \mathbf{Y})$ is Normal with mean and covariance given by

$$\hat{\mathbf{a}}_t = \hat{V}(\mathbf{a}_t) \left(\sum_{v=1}^V \frac{1}{\hat{\tau}_v^2} y_{tv} \hat{\mathbf{s}}_v + \hat{\mathbf{G}}^{-1} \hat{\boldsymbol{\alpha}} \right), \quad \hat{V}(\mathbf{a}_t) \equiv \hat{V}(\mathbf{a}) = \left(\sum_{v=1}^V \frac{1}{\hat{\tau}_v^2} [\hat{\mathbf{s}}_v \hat{\mathbf{s}}_v^\top + \hat{V}(\mathbf{s}_v)] + \hat{\mathbf{G}}^{-1} \right)^{-1}.$$

Note that $\hat{V}(\mathbf{a}_t) \equiv \hat{V}(\mathbf{a})$ is common across $t = 1, \dots, T$. At each iteration, for identifiability we rescale $\hat{\mathbf{a}}_t$ (and $\hat{V}(\mathbf{a})$) so that $\hat{\mathbf{a}}_t$ has unit variance across $t = 1, \dots, T$.

B.3 Approximate posterior of $\boldsymbol{\alpha}$

The approximate log posterior of $\boldsymbol{\alpha}$ is given by

$$\begin{aligned} \log q(\boldsymbol{\alpha} | \mathbf{Y}) &= \mathbb{E}_{\mathbf{A}, \mathbf{G}} [\log p(\mathbf{A} | \boldsymbol{\alpha}, \mathbf{G}) + \log p(\boldsymbol{\alpha})] + \text{const} \\ &= \mathbb{E}_{\mathbf{A}, \mathbf{G}} \left[\sum_{t=1}^T \log g(\mathbf{a}_t : \boldsymbol{\alpha}, \mathbf{G}) + \log g(\boldsymbol{\alpha} : \mathbf{0}, \sigma_\alpha^2 \mathbf{I}) \right] \end{aligned}$$

$$\begin{aligned}
&\propto -\frac{1}{2} \mathbb{E}_{\mathbf{A}, \mathbf{G}} \left[\sum_{t=1}^T (\mathbf{a}_t - \boldsymbol{\alpha})^\top \mathbf{G}^{-1} (\mathbf{a}_t - \boldsymbol{\alpha}) + \boldsymbol{\alpha}^\top (\sigma_\alpha^2 \mathbf{I})^{-1} \boldsymbol{\alpha} \right] \\
&\propto -\frac{1}{2} \mathbb{E}_{\mathbf{A}, \mathbf{G}} \left[-2\boldsymbol{\alpha}^\top \mathbf{G}^{-1} \sum_{t=1}^T \mathbf{a}_t + \boldsymbol{\alpha}^\top \left(\frac{1}{\sigma_\alpha^2} \mathbf{I} + T\mathbf{G}^{-1} \right) \boldsymbol{\alpha} \right] \\
&= -\frac{1}{2} \left\{ -2\boldsymbol{\alpha}^\top \mathbf{G}^{-1} \sum_{t=1}^T \hat{\mathbf{a}}_t + \boldsymbol{\alpha}^\top \left(\frac{1}{\sigma_\alpha^2} \mathbf{I} + T\hat{\mathbf{G}}^{-1} \right) \boldsymbol{\alpha} \right\}.
\end{aligned}$$

Then $q(\boldsymbol{\alpha}|\mathbf{Y})$ is Normal with mean and covariance given by

$$\hat{\boldsymbol{\alpha}} = \hat{V}(\boldsymbol{\alpha}) \hat{\mathbf{G}}^{-1} \sum_{t=1}^T \hat{\mathbf{a}}_t \quad \text{and} \quad \hat{V}(\boldsymbol{\alpha}) = \left(\frac{1}{\sigma_\alpha^2} \mathbf{I} + T\hat{\mathbf{G}}^{-1} \right)^{-1}.$$

If we let the prior variance σ_α^2 be infinite for an uninformative prior, then these simplify to $\hat{V}(\boldsymbol{\alpha}) = \hat{\mathbf{G}}/T$ and $\hat{\boldsymbol{\alpha}} = \frac{1}{T} \sum_{t=1}^T \hat{\mathbf{a}}_t$.

B.4 Approximate posterior of \mathbf{G}

Turning to \mathbf{G} , recall that $p(\mathbf{G}) \sim IW(\boldsymbol{\Psi}_0, \nu_0)$. The approximate log posterior of \mathbf{G} is given by

$$\begin{aligned}
\log q(\mathbf{G}|\mathbf{Y}) &= \mathbb{E}_{\mathbf{A}, \boldsymbol{\alpha}} [\log p(\mathbf{A}|\boldsymbol{\alpha}, \mathbf{G}) + \log p(\mathbf{G})] + \text{const} \\
&\propto -\frac{1}{2} \mathbb{E}_{\mathbf{A}, \boldsymbol{\alpha}} \left[T \log |\mathbf{G}| + \sum_{t=1}^T (\mathbf{a}_t - \boldsymbol{\alpha})^\top \mathbf{G}^{-1} (\mathbf{a}_t - \boldsymbol{\alpha}) + (\nu_0 + Q + 1) \log |\mathbf{G}| + \text{Tr} \{ \boldsymbol{\Psi}_0 \mathbf{G}^{-1} \} \right] \\
&\propto -\frac{1}{2} \mathbb{E}_{\mathbf{A}, \boldsymbol{\alpha}} \left[(T + \nu_0 + Q + 1) \log |\mathbf{G}| + \text{Tr} \left\{ \left(\sum_{t=1}^T \mathbf{a}_t \mathbf{a}_t^\top - 2\boldsymbol{\alpha} \sum_{t=1}^T \mathbf{a}_t^\top + T\boldsymbol{\alpha} \boldsymbol{\alpha}^\top + \boldsymbol{\Psi}_0 \right) \mathbf{G}^{-1} \right\} \right].
\end{aligned}$$

So $q(\mathbf{G}|\mathbf{Y}) \sim IW(\hat{\boldsymbol{\Psi}}_G, \nu_G)$ with mean $\hat{\mathbf{G}} = (\nu_G - Q - 1)^{-1} \hat{\boldsymbol{\Psi}}_G$, where $\nu_G = \nu_0 + T$ and

$$\hat{\boldsymbol{\Psi}}_G = \boldsymbol{\Psi}_0 + \sum_{t=1}^T \left(\hat{\mathbf{a}}_t \hat{\mathbf{a}}_t^\top + \hat{V}(\mathbf{a}_t) \right) - 2\hat{\boldsymbol{\alpha}} \sum_{t=1}^T \hat{\mathbf{a}}_t^\top + T \left(\hat{\boldsymbol{\alpha}} \hat{\boldsymbol{\alpha}}^\top + \hat{V}(\boldsymbol{\alpha}) \right).$$

B.5 Approximate posterior of τ

Finally for τ , the approximate posterior factorizes over v , and $\log q(\tau_v^2|\mathbf{Y})$ is given by

$$\log q(\tau_v^2|\mathbf{Y}) = \mathbb{E}_{\mathbf{A}, \mathbf{s}_v} [\log p(\mathbf{y}_v|\mathbf{A}, \mathbf{s}_v, \tau_v^2) + \log p(\tau_v^2)] + \text{const}$$

$$\begin{aligned}
&= \mathbb{E}_{\mathbf{A}, \mathbf{s}_v} \left[\sum_{t=1}^T \log g(y_{tv} : \mathbf{a}_t^\top \mathbf{s}_v) + \log p(\tau_v^2) \right] \\
&\propto \mathbb{E}_{\mathbf{A}, \mathbf{s}_v} \left[-\frac{T}{2} \log(\tau_v^2) - \frac{1}{2\tau_v^2} \sum_{t=1}^T (y_{tv} - \mathbf{a}_t^\top \mathbf{s}_v)^2 - (\alpha_0 + 1) \log(\tau_v^2) - \frac{\beta_0}{\tau_v^2} \right] \\
&= -\left(\alpha_0 + \frac{T}{2} + 1 \right) \log(\tau_v^2) - \frac{1}{\tau_v^2} \left\{ \beta_0 + \frac{1}{2} \sum_{t=1}^T y_{tv}^2 - \left(\sum_{t=1}^T y_{tv} \hat{\mathbf{a}}_t^\top \right) \hat{\mathbf{s}}_v \right. \\
&\quad \left. + \frac{1}{2} \mathbb{E}_{\mathbf{A}, \mathbf{s}_v} \left[\mathbf{s}_v^\top \left(\sum_{t=1}^T \mathbf{a}_t \mathbf{a}_t^\top \right) \mathbf{s}_v \right] \right\}.
\end{aligned}$$

Note that because the posteriors of \mathbf{A} and \mathbf{S} are assumed to factorize, the last expectation can be written as

$$\mathbb{E}_{\mathbf{s}_v} \left[\mathbf{s}_v^\top \left(\sum_{t=1}^T \hat{\mathbf{a}}_t \hat{\mathbf{a}}_t^\top + \hat{V}(\mathbf{a}_t) \right) \mathbf{s}_v \right] = Tr \left\{ \left(\sum_{t=1}^T \hat{\mathbf{a}}_t \hat{\mathbf{a}}_t^\top + \hat{V}(\mathbf{a}_t) \right) \left(\hat{\mathbf{s}}_v \hat{\mathbf{s}}_v^\top + \hat{V}(\mathbf{s}_v) \right) \right\}$$

Therefore, $q(\tau_v^2 | \mathbf{Y}) \sim IG(\alpha_v, \hat{\beta}_v)$ with mean $\hat{\tau}_v^2 = \frac{\hat{\beta}_v}{\alpha_v - 1}$, where $\alpha_v = \alpha_0 + \frac{T}{2}$ and

$$\hat{\beta}_v = \beta_0 + \frac{1}{2} \sum_{t=1}^T y_{tv}^2 - \left(\sum_{t=1}^T y_{tv} \hat{\mathbf{a}}_t^\top \right) \hat{\mathbf{s}}_v + \frac{1}{2} Tr \left\{ \sum_{t=1}^T \left(\hat{\mathbf{a}}_t \hat{\mathbf{a}}_t^\top + \hat{V}(\mathbf{a}_t) \right) \left(\hat{\mathbf{s}}_v \hat{\mathbf{s}}_v^\top + \hat{V}(\mathbf{s}_v) \right) \right\}.$$

The evidence lower bound (ELBO) convergence criterion is defined as

$$ELBO(q) = \mathbb{E} [\log q(\mathbf{Z} | \mathbf{Y})] - \mathbb{E} [\log p(\mathbf{Y}, \mathbf{Z})] = \mathbb{E} [\log q(\mathbf{Z} | \mathbf{Y})] - \mathbb{E} [\log p(\mathbf{Y} | \mathbf{Z})] - \mathbb{E} [\log p(\mathbf{Z})],$$

where the expectation is over the approximate posterior $q(\mathbf{Z} | \mathbf{Y})$. Beginning with the first term,

$$\begin{aligned}
\mathbb{E} [\log q(\mathbf{Z} | \mathbf{Y})] &= \mathbb{E} [\log q(\mathbf{S} | \mathbf{Y}) q(\mathbf{A} | \mathbf{Y}) q(\boldsymbol{\alpha} | \mathbf{Y}) q(\mathbf{G} | \mathbf{Y}) q(\boldsymbol{\tau} | \mathbf{Y})] \\
&= \mathbb{E} \left[\sum_{v=1}^V \log q(\mathbf{s}_v | \mathbf{Y}) + \sum_{t=1}^T \log q(\mathbf{a}_t | \mathbf{Y}) + \log q(\boldsymbol{\alpha} | \mathbf{Y}) + \log q(\mathbf{G} | \mathbf{Y}) + \sum_{v=1}^V \log q(\tau_v^2 | \mathbf{Y}) \right] \\
&= \sum_{v=1}^V \log g(\hat{\mathbf{s}}_v : \hat{\mathbf{s}}_v, \hat{V}(\mathbf{s}_v)) + \sum_{t=1}^T \log g(\hat{\mathbf{a}}_t : \hat{\mathbf{a}}_t, \hat{V}(\mathbf{a}_t)) + \log g(\hat{\boldsymbol{\alpha}} : \hat{\boldsymbol{\alpha}}, \hat{V}(\boldsymbol{\alpha})) \\
&\quad + \log h_{IW}(\hat{\mathbf{G}} : \hat{\boldsymbol{\Psi}}_G, \nu_G) + \sum_{v=1}^V \log h_{IG}(\hat{\tau}_v^2 : \alpha_v, \hat{\beta}_v) \\
&\propto -\frac{1}{2} \sum_{v=1}^V \log |\hat{V}(\mathbf{s}_v)| - \frac{T}{2} \log |\hat{V}(\mathbf{a}_t)| - \frac{1}{2} \log |\hat{V}(\boldsymbol{\alpha})|
\end{aligned}$$

$$\begin{aligned}
& -\frac{1}{2}(\nu_0 + T + Q + 1) \mathbb{E} [\log |\mathbf{G}|] - \frac{1}{2} \text{Tr} \left\{ \hat{\Psi}_{\mathbf{G}} \mathbb{E}[\mathbf{G}^{-1}] \right\} \\
& - (\alpha_0 + T/2 + 1) \sum_{v=1}^V \mathbb{E} [\log(\tau_v^2)] - \sum_{v=1}^V \hat{\beta}_v \mathbb{E} [1/\tau_v^2].
\end{aligned}$$

Turning to the second term, $\mathbb{E} [\log p(\mathbf{Y}|\mathbf{Z})] = \sum_{v=1}^V \mathbb{E} [\log g(\mathbf{y}_v : \mathbf{A}\mathbf{s}_v, \tau_v^2 \mathbf{I}_T)]$, for each $v = 1, \dots, V$, the summand is

$$\begin{aligned}
& -\frac{1}{2} \left[T \mathbb{E} [\log(\tau_v^2)] + \mathbb{E} [1/\tau_v^2] \left(\sum_{t=1}^T y_{tv} - 2 \sum_{t=1}^T y_{tv} \hat{\mathbf{a}}_t^\top \hat{\mathbf{s}}_v + \text{Tr} \left\{ \sum_{t=1}^T \mathbb{E} [\mathbf{a}_t \mathbf{a}_t^\top] \mathbb{E} [\mathbf{s}_v \mathbf{s}_v^\top] \right\} \right) \right] \\
& = -\frac{1}{2} \left[T \mathbb{E} [\log(\tau_v^2)] + \mathbb{E} [1/\tau_v^2] \left(\sum_{t=1}^T y_{tv} - 2 \sum_{t=1}^T y_{tv} \hat{\mathbf{a}}_t^\top \hat{\mathbf{s}}_v \right. \right. \\
& \quad \left. \left. + \text{Tr} \left\{ \sum_{t=1}^T (\hat{\mathbf{a}}_t \hat{\mathbf{a}}_t^\top + \hat{V}(\mathbf{a}_t)) (\hat{\mathbf{s}}_v \hat{\mathbf{s}}_v^\top + \hat{V}(\mathbf{s}_v)) \right\} \right) \right] \\
& = -\frac{1}{2} \left[T \mathbb{E} [\log(\tau_v^2)] + 2 \mathbb{E} [1/\tau_v^2] (\hat{\beta}_v - \beta_0) \right],
\end{aligned}$$

since $\hat{\beta}_v = \beta_0 + \frac{1}{2} \sum_{t=1}^T y_{tv}^2 - \left(\sum_{t=1}^T y_{tv} \hat{\mathbf{a}}_t^\top \right) \hat{\mathbf{s}}_v + \frac{1}{2} \text{Tr} \left\{ \sum_{t=1}^T (\hat{\mathbf{a}}_t \hat{\mathbf{a}}_t^\top + \hat{V}(\mathbf{a}_t)) (\hat{\mathbf{s}}_v \hat{\mathbf{s}}_v^\top + \hat{V}(\mathbf{s}_v)) \right\}$.

Turning to the third term,

$$\begin{aligned}
\mathbb{E} [\log p(\mathbf{Z})] & = \mathbb{E} [\log p(\mathbf{S})p(\mathbf{A})p(\mathbf{G})p(\boldsymbol{\alpha})p(\boldsymbol{\tau})] \\
& = \mathbb{E} \left[\sum_{v,q} \log p(s_{q,v}) + \sum_{t=1}^T \log p(\mathbf{a}_t) + \sum_{q=1}^Q \log p(\alpha_q) + \log p(\mathbf{G}) + \sum_{v=1}^V \log p(\tau_v^2) \right] \\
& = \mathbb{E} \left[\sum_{v,q} \log q(s_{q,v} : s_{q,v}^0, \sigma_{q,v}^2) + \sum_{t=1}^T \log g(\mathbf{a}_t : \boldsymbol{\alpha}, \mathbf{G}) \right. \\
& \quad \left. + \sum_{q=1}^Q \log g(\alpha_q : 0, \sigma_\alpha^2) + \log h_{IW}(\mathbf{G} : \Psi_0, \nu_0) + \sum_{v=1}^V \log h_{IG}(\tau_v^2 : \alpha_0, \beta_0) \right] \\
& \propto -\frac{1}{2} \left[\sum_{v=1}^V \sum_{q=1}^Q \frac{1}{\sigma_{q,v}^2} (\mathbb{E}[s_{q,v}^2] - 2s_{q,v}^0 \hat{s}_{q,v}) + T \mathbb{E}[\log |\mathbf{G}|] \right. \\
& \quad \left. + \text{Tr} \left\{ \mathbb{E}[\mathbf{G}^{-1}] \left(\sum_{t=1}^T \mathbb{E}[\mathbf{a}_t \mathbf{a}_t^\top] - 2\hat{\boldsymbol{\alpha}} \sum_{t=1}^T \hat{\mathbf{a}}_t + T \mathbb{E}[\boldsymbol{\alpha} \boldsymbol{\alpha}^\top] \right) \right\} + \frac{1}{\sigma_\alpha^2} \mathbb{E}[\boldsymbol{\alpha} \boldsymbol{\alpha}^\top] \right. \\
& \quad \left. + (\nu_0 + Q + 1) \mathbb{E}[\log |\mathbf{G}|] + \text{Tr} \left\{ \mathbb{E}[\mathbf{G}^{-1}] \Psi_0 \right\} \right]
\end{aligned}$$

$$\begin{aligned}
& -(\alpha_0 + 1) \sum_{v=1}^V \mathbb{E}[\log(\tau_v^2)] - \beta_0 \sum_{v=1}^V \mathbb{E}[1/\tau_v^2] \\
= & -\frac{1}{2} \left[\sum_{v=1}^V \sum_{q=1}^Q \frac{1}{\sigma_{q,v}^2} \left(\hat{V}(s_{q,v}) + \hat{s}_{q,v}^2 - 2s_{q,v}^0 \hat{s}_{q,v} \right) \right. \\
& \left. + (T + \nu_0 + Q + 1) \mathbb{E}[\log |\mathbf{G}|] + \text{Tr} \left\{ \mathbb{E}[\mathbf{G}^{-1}] \hat{\Psi}_G \right\} \right] \\
& -(\alpha_0 + 1) \sum_{v=1}^V \mathbb{E}[\log(\tau_v^2)] - \beta_0 \sum_{v=1}^V \mathbb{E}[1/\tau_v^2]
\end{aligned}$$

since $\hat{\Psi}_G = \Psi_0 + \sum_{t=1}^T (\hat{\mathbf{a}}_t \hat{\mathbf{a}}_t^\top + \hat{V}(\mathbf{a}_t)) - 2\hat{\boldsymbol{\alpha}} \sum_{t=1}^T \hat{\mathbf{a}}_t^\top + T(\hat{\boldsymbol{\alpha}} \hat{\boldsymbol{\alpha}}^\top + \hat{V}(\boldsymbol{\alpha}))$, and the term involving the prior variance on $\boldsymbol{\alpha}$, σ_α^2 , goes to zero as that variance is assumed to be large.

Combining the three terms, the terms involving $\mathbb{E}[\log |\mathbf{G}|]$, $\mathbb{E}[\mathbf{G}^{-1}]$, $\mathbb{E}[\log(\tau_v^2)]$, and $\mathbb{E}[1/\tau_v^2]$ all cancel out, and we are left with

$$\begin{aligned}
ELBO(q) \propto & -\frac{1}{2} \sum_{v=1}^V \log |\hat{V}(\mathbf{s}_v)| - \frac{T}{2} \log |\hat{V}(\mathbf{a})| - \frac{1}{2} \log |\hat{V}(\boldsymbol{\alpha})| \\
& + \frac{1}{2} \sum_{v=1}^V \sum_{q=1}^Q \frac{1}{\sigma_{q,v}^2} \left(\hat{V}(s_{q,v}) + \hat{s}_{q,v}^2 - 2s_{q,v}^0 \hat{s}_{q,v} \right)
\end{aligned}$$

C Additional Simulation Figures

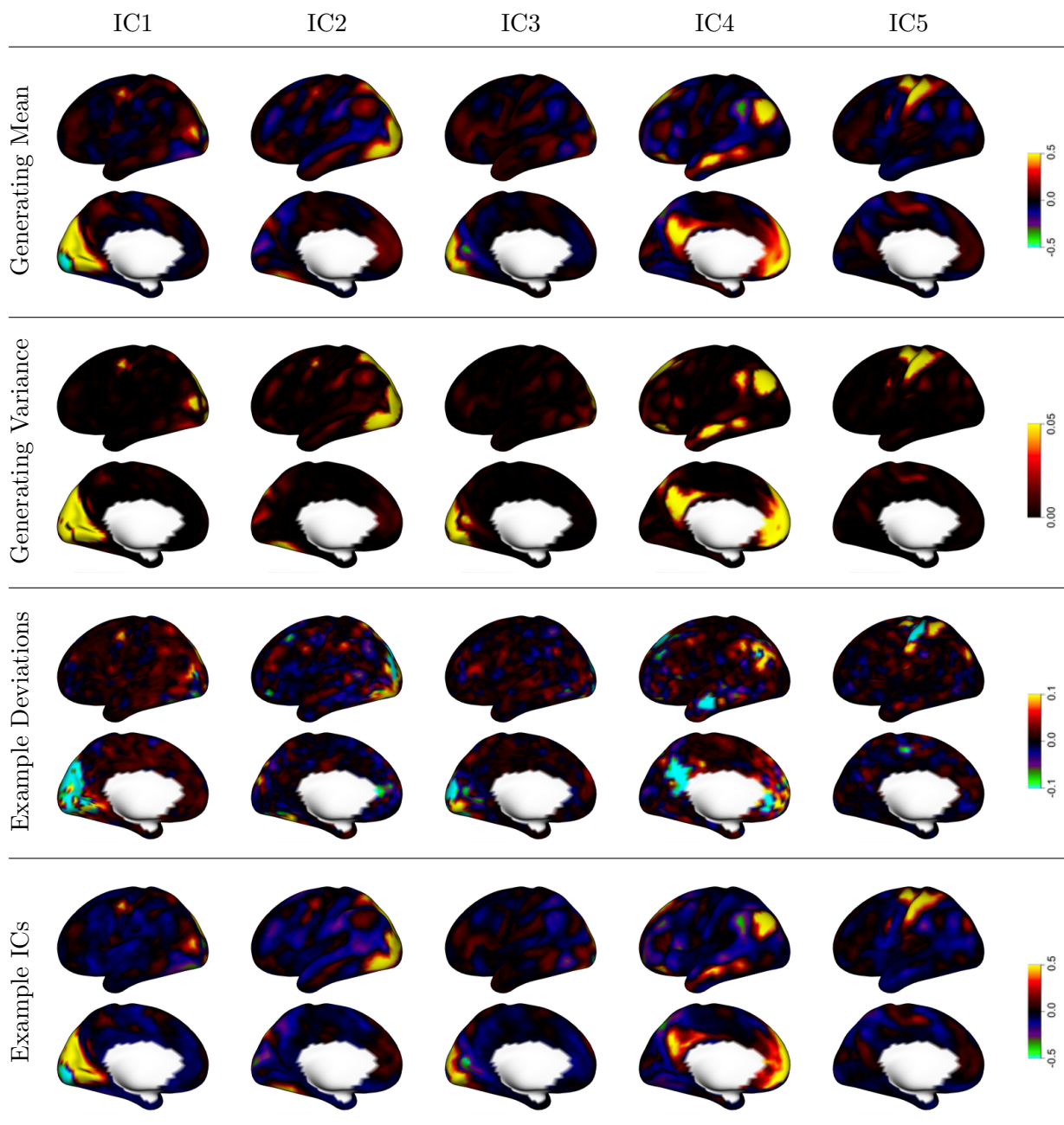


Figure C.1: Generation of simulated subject-level IC maps. Unique subject-level deviation maps (third row) are created by generating mean-zero Normal draws with variance equal to the generating variance, then spatially smoothing the resulting maps along the surface. Unique subject-level IC maps (fourth row) are created by adding those deviation maps to the generating mean maps. The result is subject-specific ICs that are similar to the group-average ICs but with subtle differences.

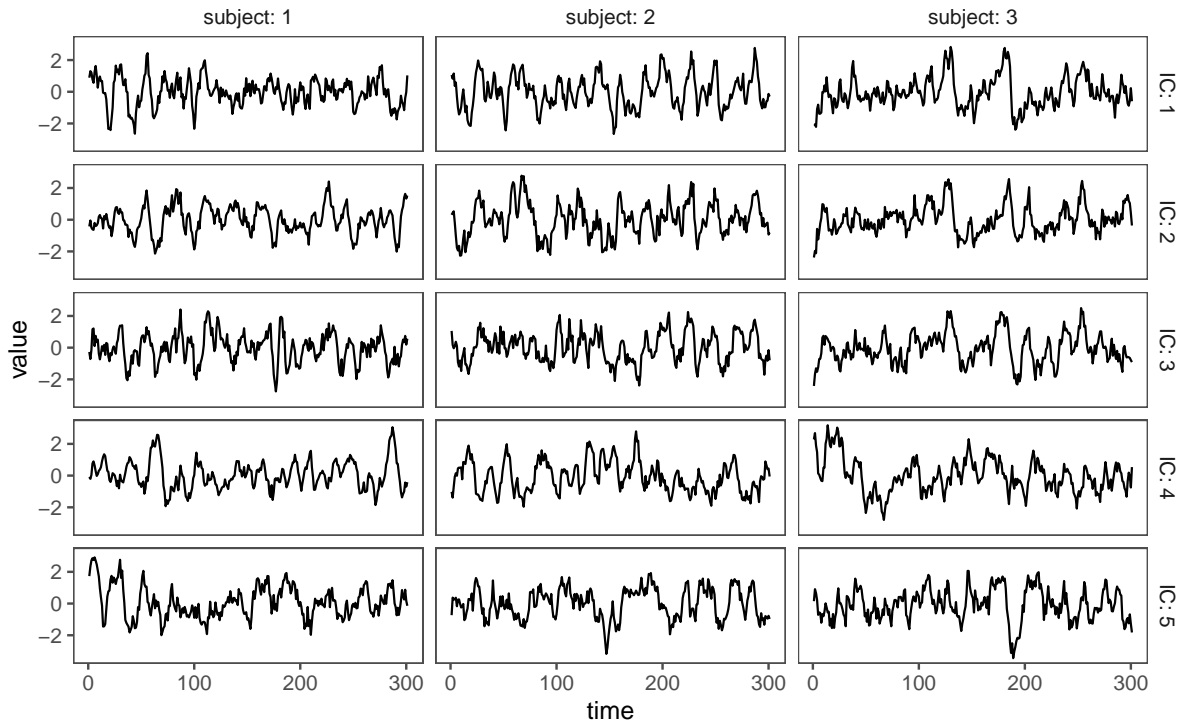


Figure C.2: True IC time courses and functional connectivity (FC) for three example subjects in simulation study. The time courses (arbitrary units) are based on real fMRI data and exhibit realistic features like autocorrelation. Only 300 of the total 1200 time points are shown. The FC matrices (based on all 1200 time points) show similar but unique patterns across the subjects.

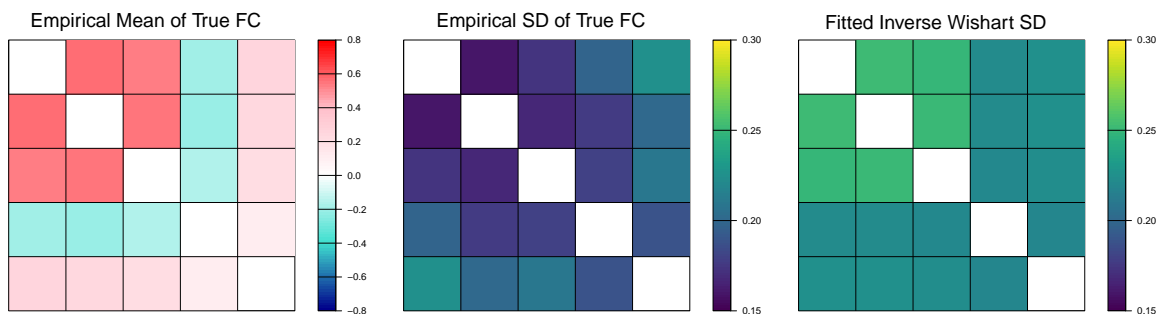


Figure C.3: Empirical mean and standard deviation of functional connectivity (FC) alongside inverse Wishart standard deviation in the simulation study.

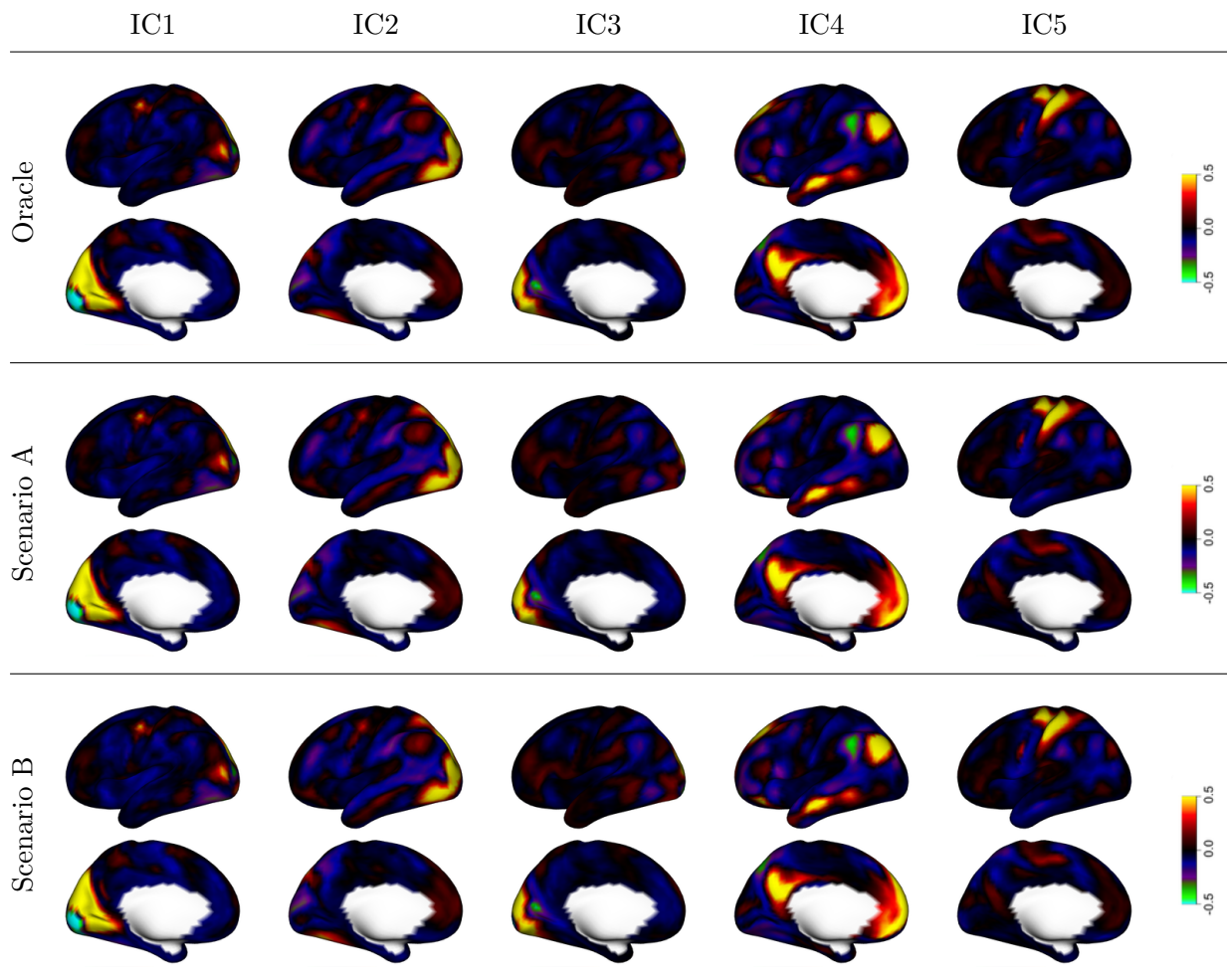


Figure C.4: Prior mean for spatial IC maps in simulation study. The oracle mean values are given by the empirical mean of the true spatial IC maps; the estimated mean values in Scenarios A and B are based on extraction of the latent signals from the fMRI timeseries as described in Section 2.1. In both scenarios, the estimated means are a very close approximation of the true means. Note that the mean across ICs is very similar to the generating mean shown in Figure C.1.

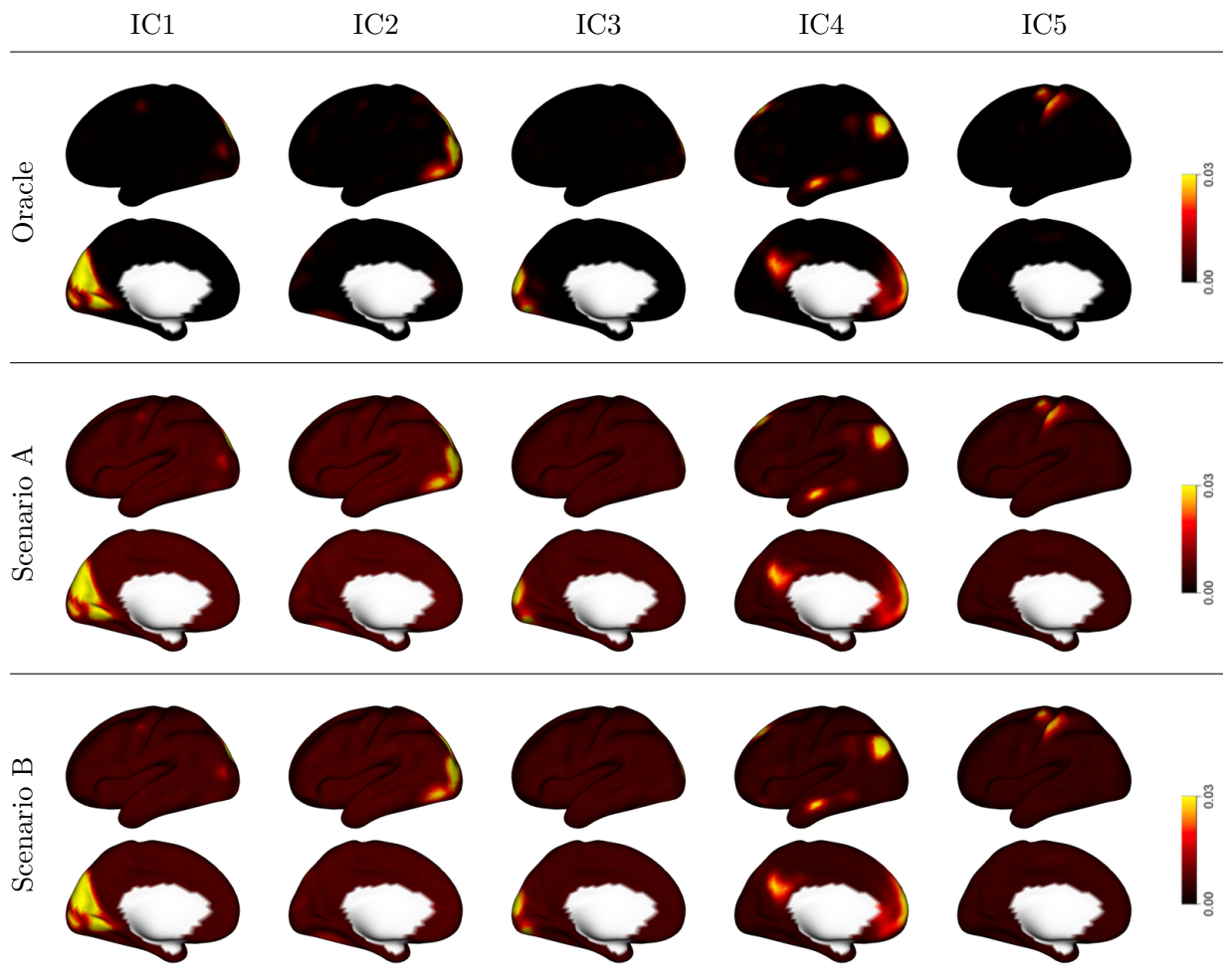


Figure C.5: Prior variance for spatial IC maps in simulation study. The oracle variance values are given by the empirical variance of the true spatial IC maps; the estimated variance values in Scenarios A and B are based on extraction of the latent signals from the fMRI timeseries as described in Section 2.1. The estimated variances are very similar to the oracle variances in higher-variance regions, but are notably higher than the oracle variance in background (low-variance) areas. This is a result of the biased non-negative variance estimation approach, which avoids under-estimation of the variance for a less informative prior. Note that the true variance across ICs is smaller than the generating variance shown in Figure C.1, due to the spatial smoothing step during subject-level IC generation.

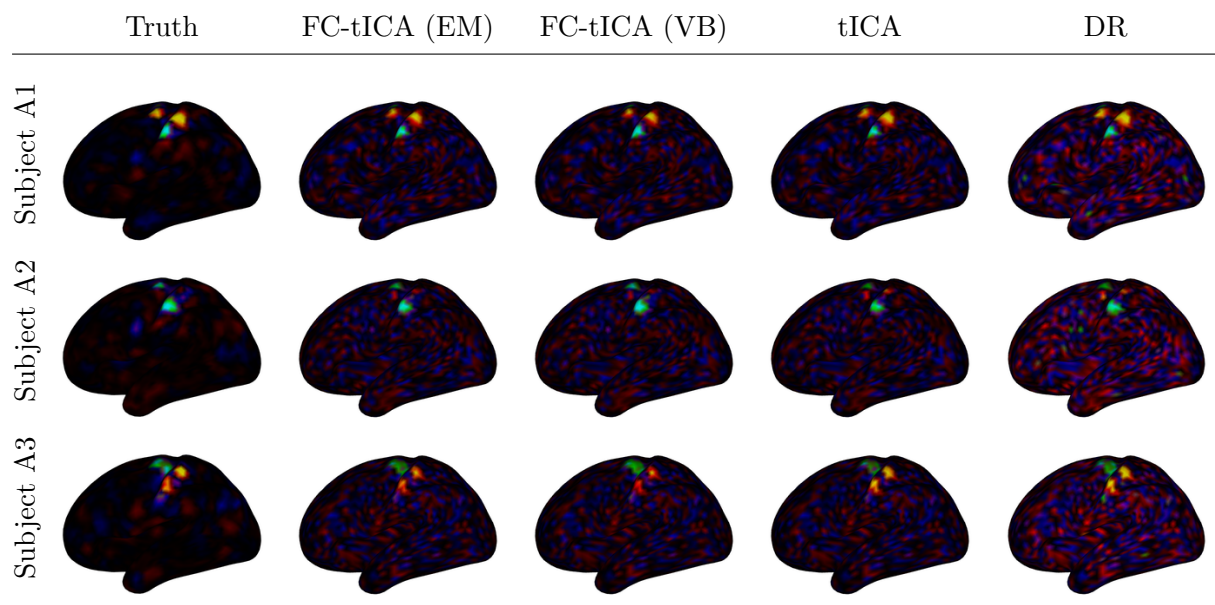


Figure C.6: Estimated subject-level deviations in simulation scenario A. For three randomly selected test subjects, the true and estimated deviation maps for the motor IC (IC 5) are shown. The two proposed algorithms for FC template ICA (FC-tICA) and the existing methods tICA and DR all identify the unique features of each subject reasonably well. The DR estimates are noticeably noisier.

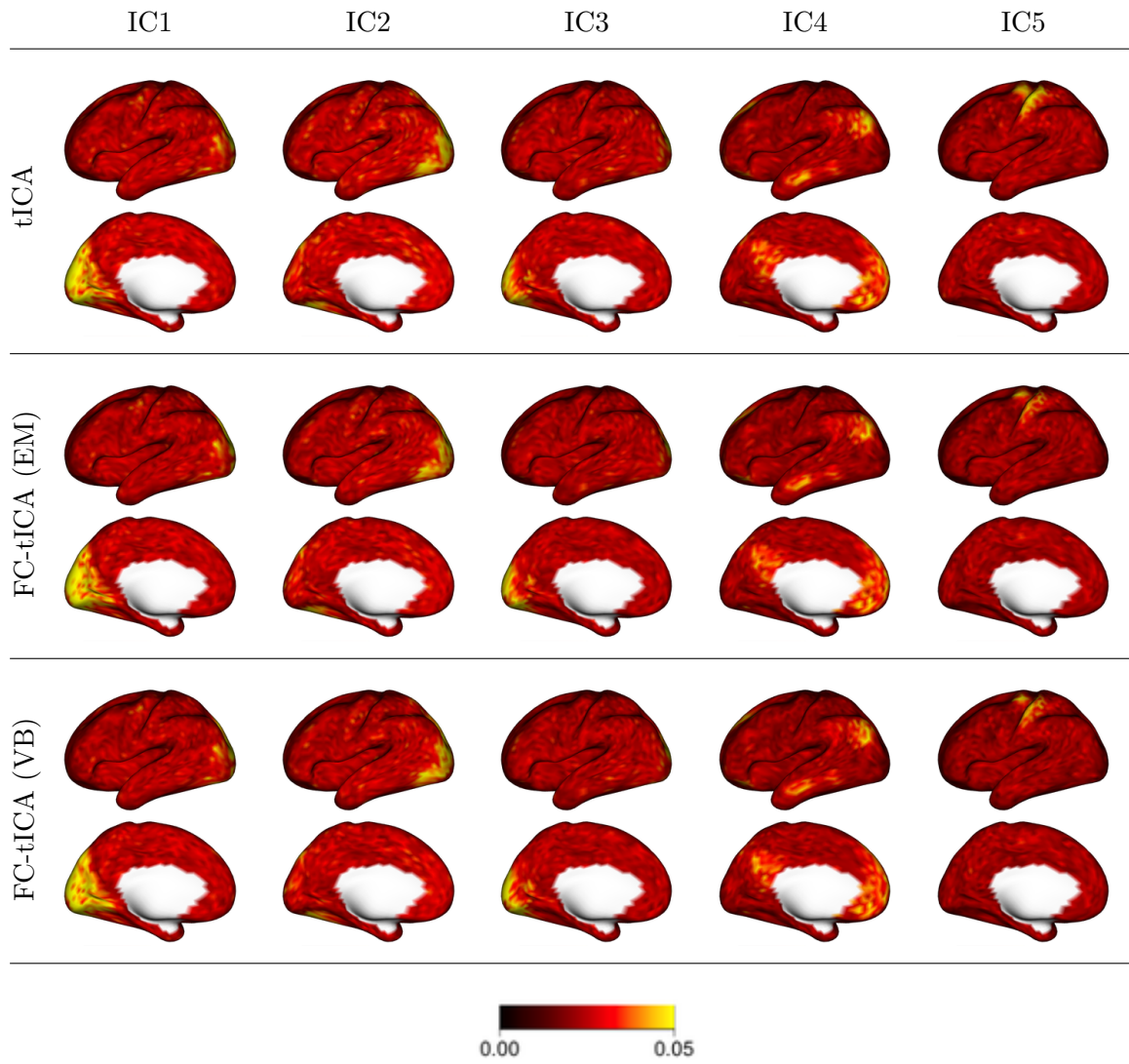


Figure C.7: Median absolute error (MAE) of estimated subject-level spatial maps over 50 simulated test subjects in simulation scenario A. Similar patterns are seen across the algorithms, with lower error in background areas and higher error in the areas of engagement for this IC.

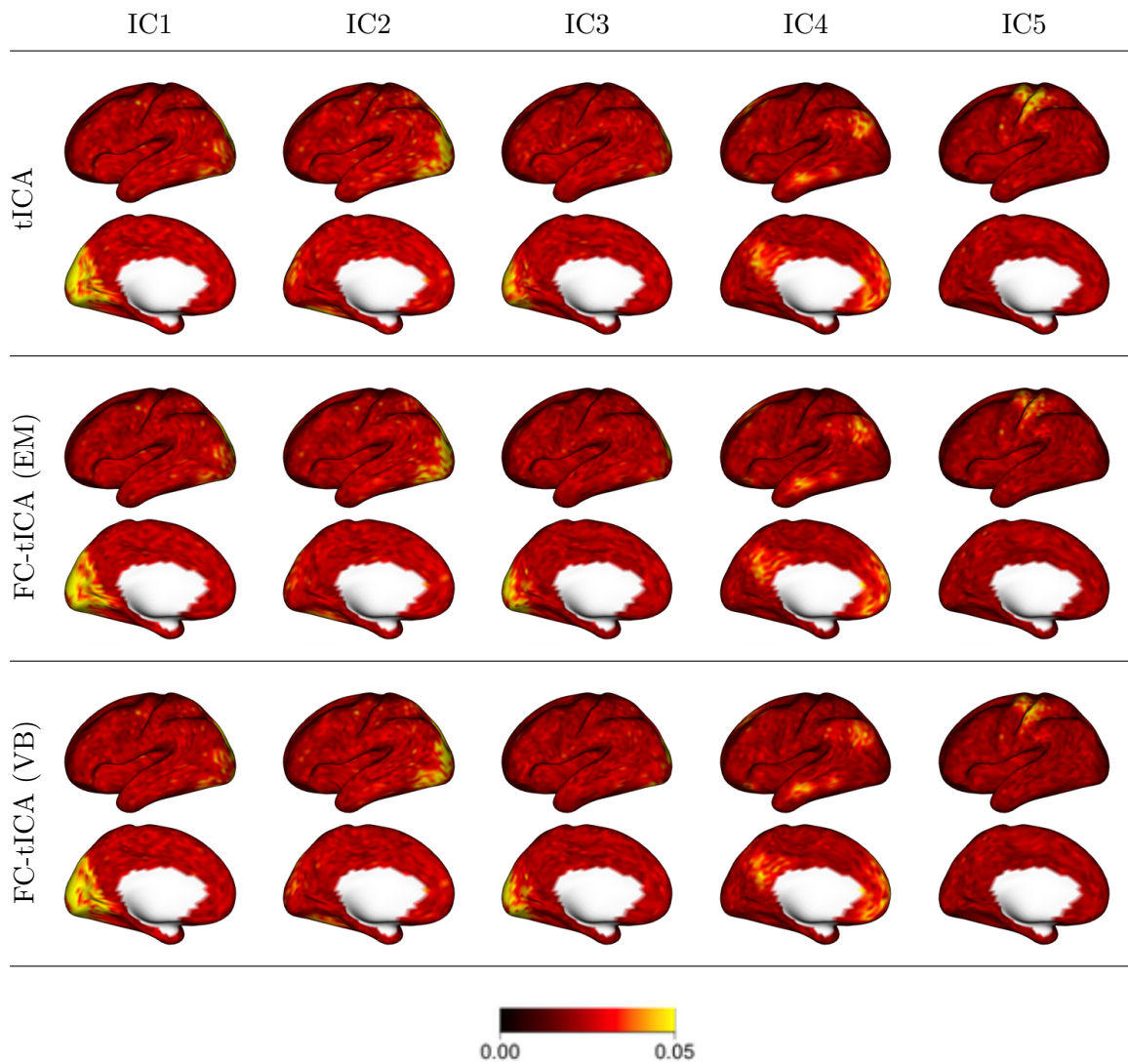


Figure C.8: Median absolute error (MAE) of estimated subject-level spatial maps over 50 simulated test subjects in simulation scenario B.

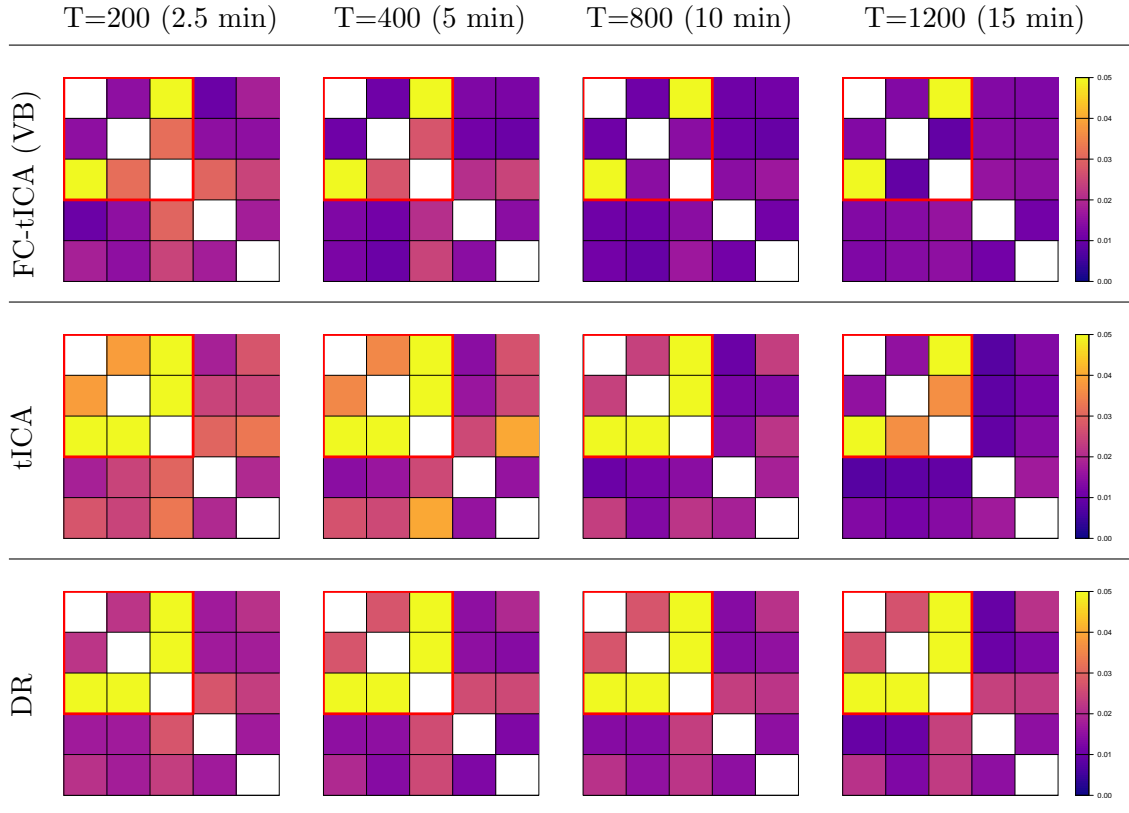


Figure C.9: Accuracy of FC estimates by fMRI scan duration in simulation scenario B. Values shown are median absolute error (MAE) across 50 test subjects. The proposed FC-tICA VB algorithm clearly outperforms the existing methods template ICA (tICA) and dual regression (DR), particularly for shorter durations.

D Additional Data Analysis Tables and Figures

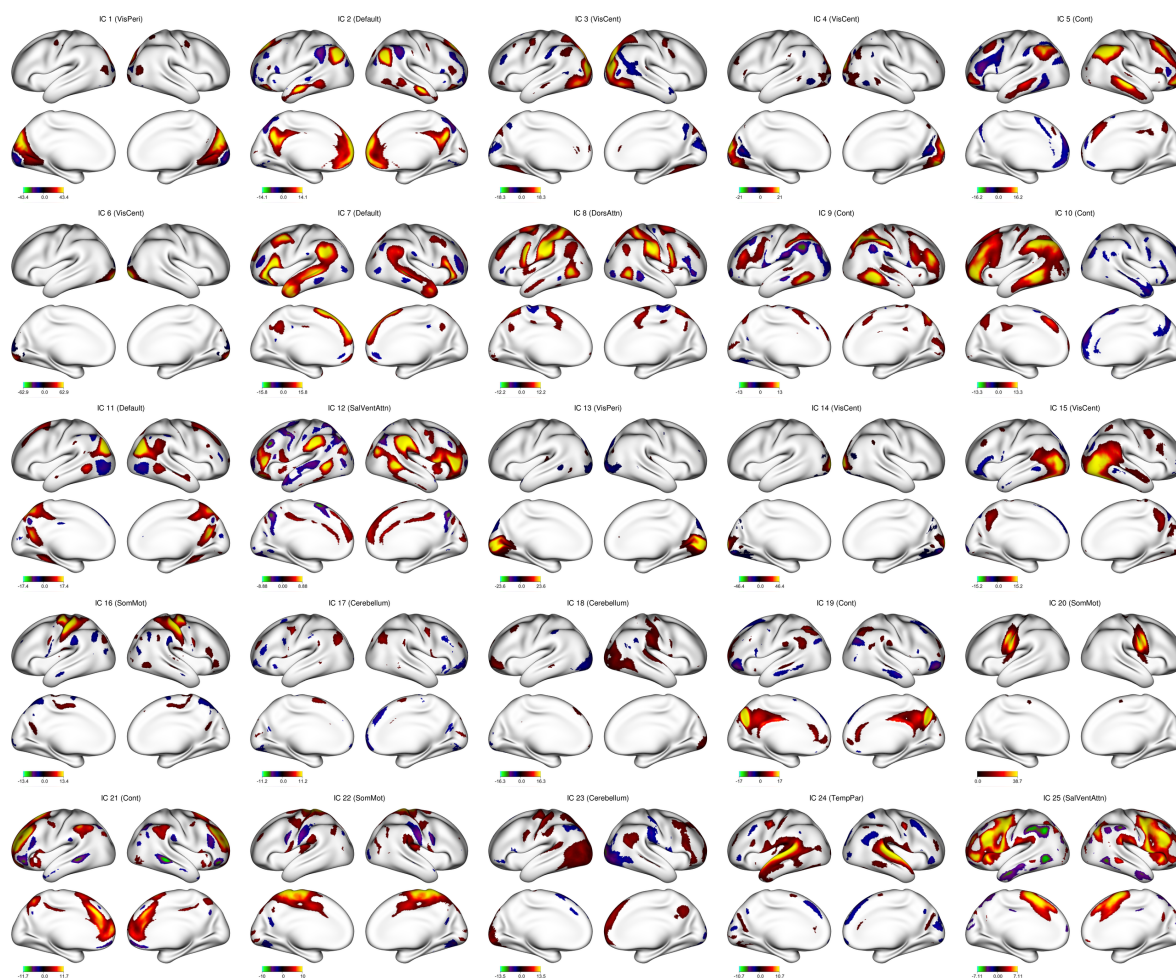


Figure D.10: Thresholded group IC maps and network assignments for low-resolution ($Q = 25$) ICA in HCP data analysis. Only the cortical surface part of each map is shown here. See Figure D.11 for subcortical views.

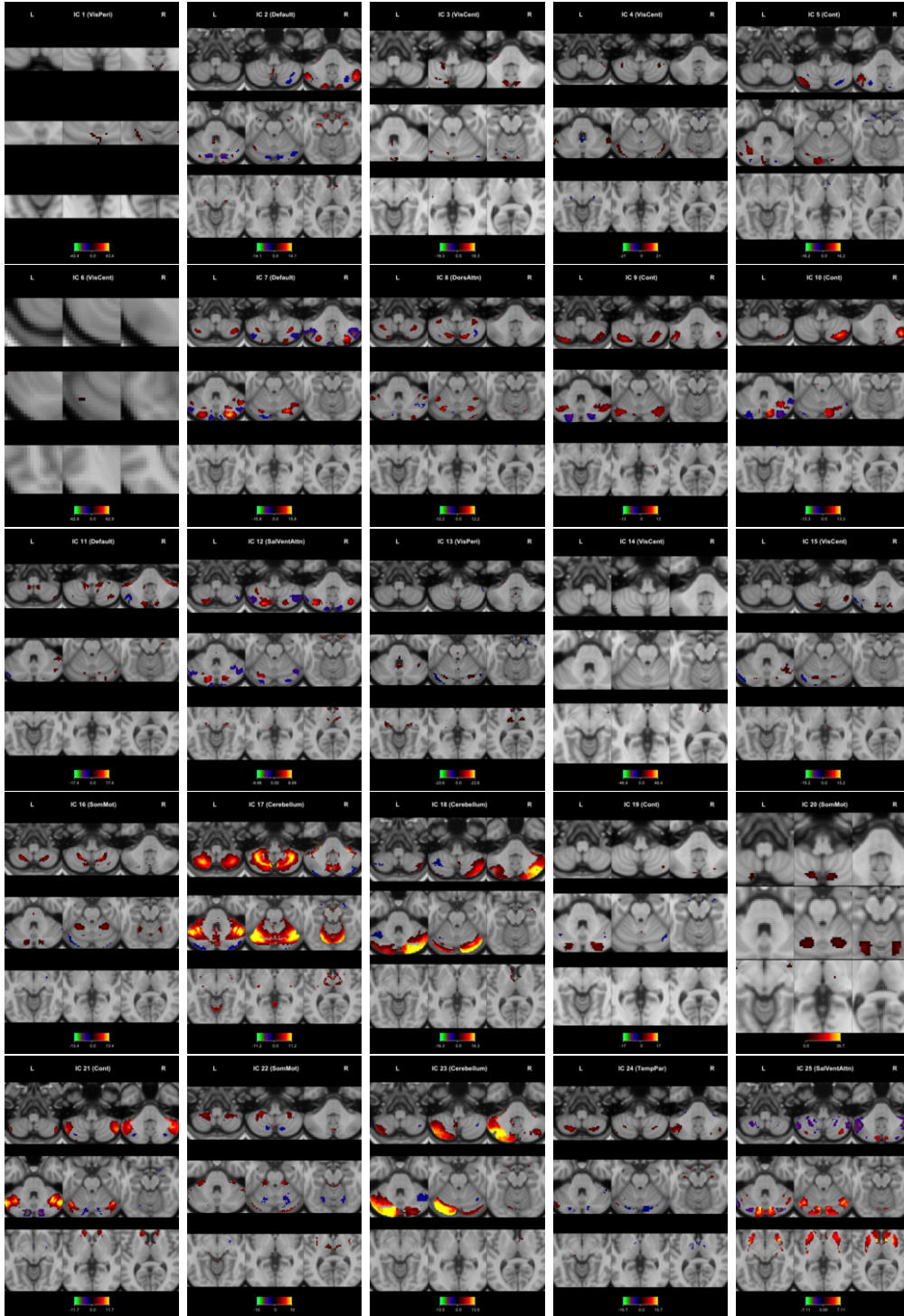


Figure D.11: Thresholded group IC maps and network assignments for low-resolution ($Q = 25$) ICA in HCP data analysis. Only the subcortical part of each map is shown here. See Figure D.10 for cortical views.

RSN or Parcel Name	Group Name	# of ICs ($Q = 25$)	# of ICs ($Q = 100$)
Visual (Central)	V	5	13
Visual (Peripheral)	V	2	3
Somatomotor	M	3	7
Dorsal Attention	A	1	6
Ventral Attention	A	2	4
Limbic	L	0	1
Control	C	5	12
Default	D	3	13
Temporal Parietal	TP	1	3
Brain Stem	B	0	6
Cerebellum	CB	3	27
Accumbens	SUB	0	1
Amygdala	SUB	0	2
Caudate	SUB	0	1
Hippocampus	SUB	0	1
Putamen	SUB	0	1
Thalamus	SUB	0	1

Table D.1: Number of group ICs assigned to each resting-state network (RSN) or subcortical parcel in HCP data analysis. The second column shows the short group name, used to order and label the FC matrices shown in subsequent figures. Note that in the low-resolution ICA a single IC represents the cerebellum and no subcortical ICs appear, while in the high-resolution ICA there are many cerebellar and subcortical ICs. In addition, nearly all of the cortical RSNs are represented by a larger number of ICs in the high-resolution ICA versus the low-resolution ICA, reflecting a finer scale representation of functional brain areas.

IC	RSN or Parcel
3	VisCent
4	VisCent
6	VisCent
14	VisCent
15	VisCent
1	VisPeri
13	VisPeri
16	SomMot
20	SomMot
22	SomMot
8	DorsAttn
12	SalVentAttn
25	SalVentAttn
5	Cont
9	Cont
10	Cont
19	Cont
21	Cont
2	Default
7	Default
11	Default
24	TempPar
17	Cerebellum
18	Cerebellum
23	Cerebellum

Table D.2: Group ICs assigned to each resting-state network (RSN) or subcortical parcel in HCP data analysis for $Q = 25$.

IC	RSN or Parcel	IC	RSN or Parcel	IC	RSN or Parcel
1	VisCent	75	Limbic	100	Brain Stem
4	VisCent	3	Cont	41	Cerebellum
5	VisCent	11	Cont	49	Cerebellum
7	VisCent	20	Cont	59	Cerebellum
9	VisCent	24	Cont	61	Cerebellum
12	VisCent	32	Cont	63	Cerebellum
13	VisCent	43	Cont	64	Cerebellum
14	VisCent	52	Cont	65	Cerebellum
16	VisCent	53	Cont	67	Cerebellum
18	VisCent	55	Cont	68	Cerebellum
25	VisCent	56	Cont	69	Cerebellum
31	VisCent	62	Cont	70	Cerebellum
38	VisCent	66	Cont	73	Cerebellum
2	VisPeri	15	Default	76	Cerebellum
6	VisPeri	21	Default	77	Cerebellum
10	VisPeri	26	Default	78	Cerebellum
8	SomMot	28	Default	82	Cerebellum
17	SomMot	35	Default	83	Cerebellum
27	SomMot	36	Default	85	Cerebellum
30	SomMot	37	Default	86	Cerebellum
39	SomMot	42	Default	88	Cerebellum
46	SomMot	47	Default	89	Cerebellum
58	SomMot	48	Default	90	Cerebellum
19	DorsAttn	51	Default	91	Cerebellum
29	DorsAttn	71	Default	92	Cerebellum
33	DorsAttn	80	Default	93	Cerebellum
34	DorsAttn	45	TempPar	94	Cerebellum
40	DorsAttn	57	TempPar	95	Cerebellum
44	DorsAttn	60	TempPar	72	Hippocampus
22	SalVentAttn	96	Brain Stem	79	Putamen
23	SalVentAttn	97	Brain Stem	87	Putamen
50	SalVentAttn	98	Brain Stem	81	Caudate
54	SalVentAttn	99	Brain Stem	84	Thalamus

Table D.3: Group ICs assigned to each resting-state network (RSN) or subcortical parcel in HCP data analysis for $Q = 100$. IC 74 was determined to be a noise component and was not assigned to any network.

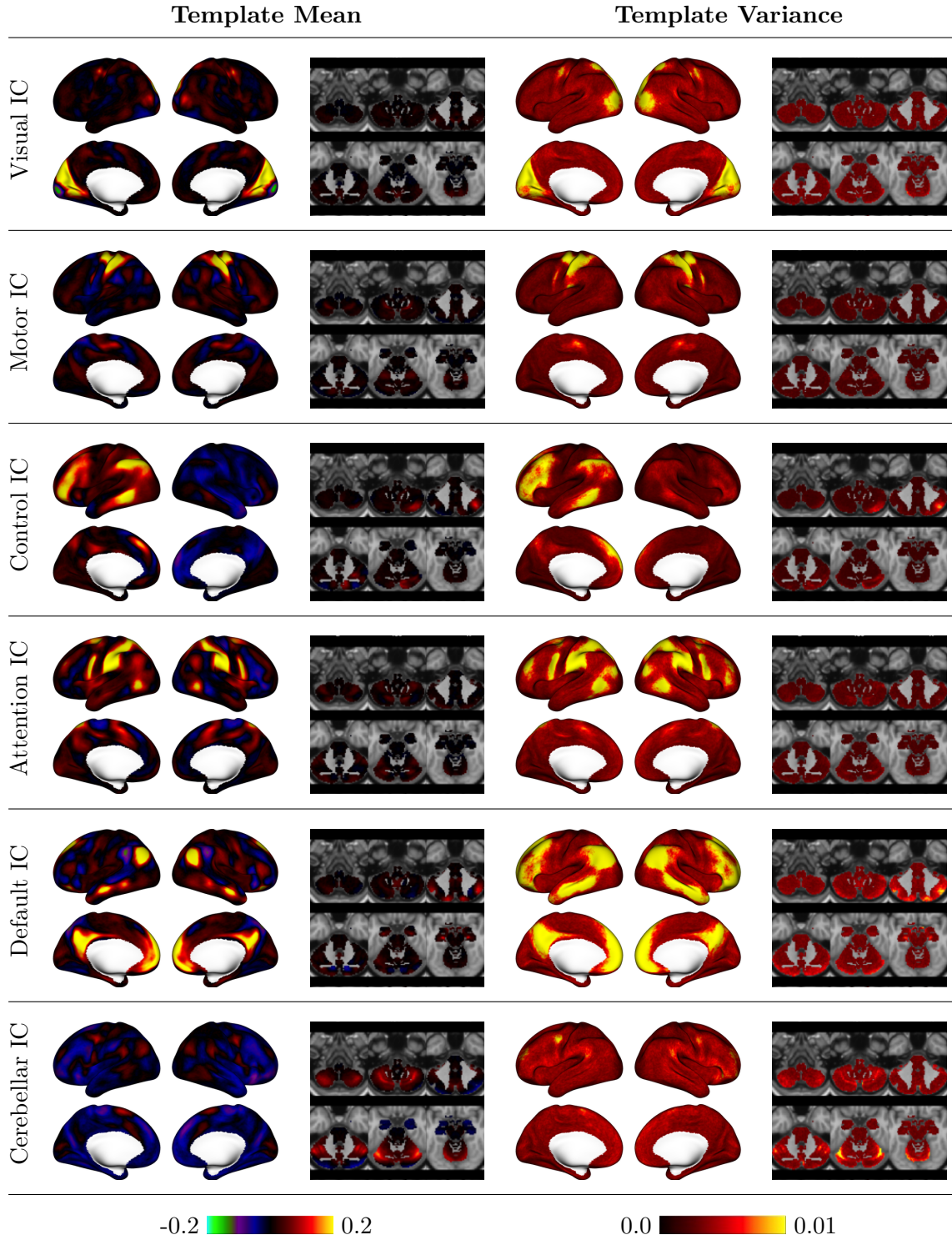


Figure D.12: Prior spatial mean and variance maps for several ICs assigned to different resting-state networks in the low-resolution ICA ($Q = 25$) in HCP data analysis.

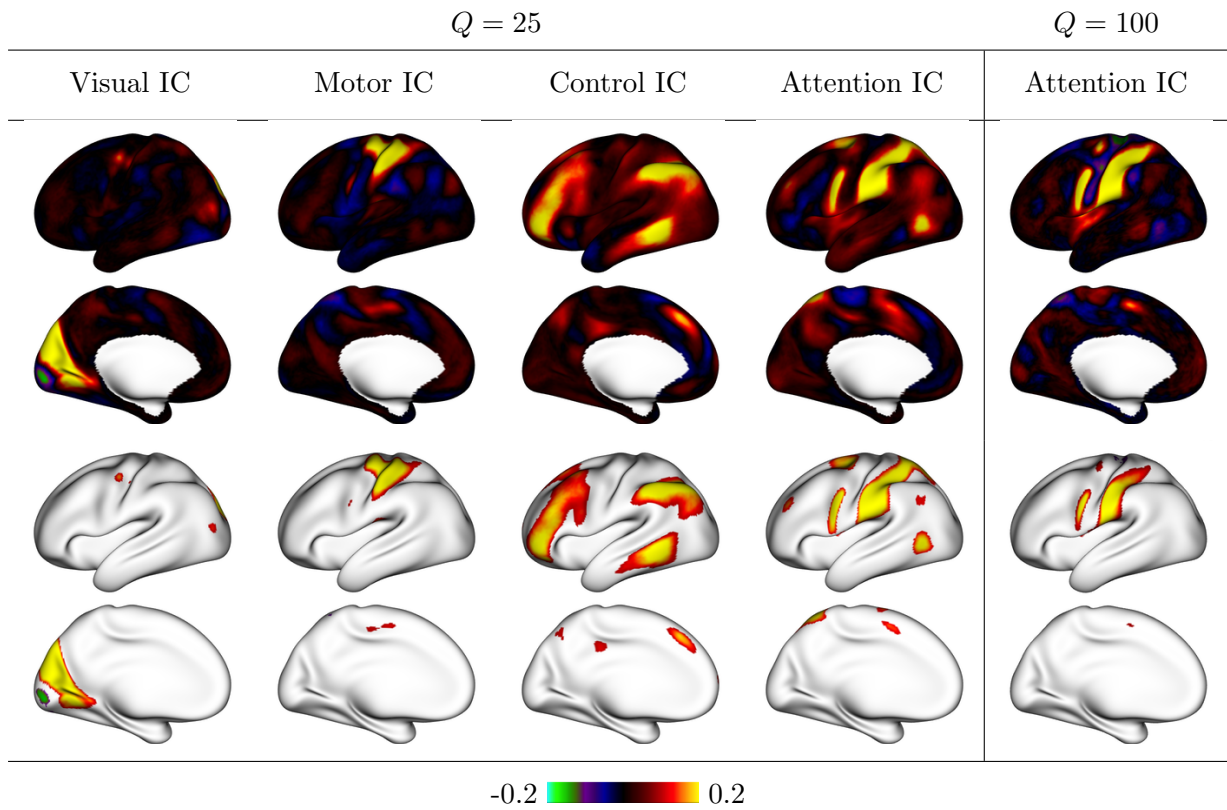


Figure D.13: Prior mean maps in HCP data analysis, before and after thresholding at the minimum effect size utilized in hypothesis testing to identify areas of statistically and scientifically significant engagement in each subject. The threshold is set to twice the spatial standard deviation of each prior mean map. The attention ICs displayed in Figure 9 and 11 are shown in the last two columns.